JOURNAL OF PETROLOGY | VOLUME 43 | NUMBER 11 | PAGES 2075–2095 | 2002

Anatectic Migmatites from the Roof of an Ocean Ridge Magma Chamber

K. M. GILLIS[1]* AND L. A. COOGAN[2]

[1]SCHOOL OF EARTH AND OCEAN SCIENCES, PO BOX 3055, UNIVERSITY OF VICTORIA, VICTORIA, B.C., CANADA V8W 3P6

[2]DEPARTMENT OF EARTH SCIENCES, CARDIFF UNIVERSITY, CARDIFF CF10 3YE, UK

RECEIVED JULY 10, 2001; REVISED TYPESCRIPT ACCEPTED MAY 14, 2002

A well-preserved contact aureole at the base of the sheeted dyke complex in the Troodos ophiolite, Cyprus, records the partial melting of the roof of a mid-ocean ridge magma chamber. Hydrothermally altered dykes within the lowermost 10–30 m of the sheeted dyke complex were recrystallized to pyroxene and hornblende hornfels and, closest to the underlying gabbros (<10 m), partially melted (up to >30%) at water-undersaturated conditions and temperatures ≥ 875°C. Geological considerations indicate that the duration of melting events was probably on the time scale of eruptive cycles (i.e. years to centuries). This resulted in disequilibrium partial melting and highly imperfect melt segregation within the contact aureole. We hypothesize that partial melting is a common process within the roof zones of axial magma chambers at fast-spreading ridges and that a component of geophysically imaged axial magma chambers may be partially melted upper crust rather than partially crystallized magma. Field relations suggest that where the highest degrees of melting occurred, a mixture of anhydrous hornfels and hydrous leucocratic melt disaggregrated, and was assimilated into the magma chamber.

KEY WORDS: *partial melting; mid-ocean ridge; axial magma chamber; Troodos ophiolite; contact metamorphism*

INTRODUCTION

At mid-ocean ridges (MORs), a critical interface for heat and mass exchange between the lithosphere and hydrosphere is the magma–hydrothermal transition. At fast-spreading MORs, where shallow axial magma chambers (AMCs) are nearly steady-state features, this interface is likely to be centred at, or very close to, the sheeted dyke–gabbro boundary. This region of the crust is a dynamic environment that is subjected to rapid changes in rheology and thermal structure. It is here that melt is episodically extracted to build the upper crust (e.g. Delaney *et al.*, 1998), crystals are precipitated to build some, if not all, of the lower crust (e.g. Phipps Morgan & Chen, 1993; Quick & Denlinger, 1993; Boudier *et al.*, 1996), and magmatic heat is rapidly transferred across a thin (<100 m) conductive boundary layer (e.g. Lowell & Burnell, 1991) and advectively transported out of the crust by hydrothermal fluids (e.g. Cann *et al.*, 1985). Geophysical surveys along the East Pacific Rise (EPR) provide indirect evidence that the depth and internal properties (e.g. melt volumes, proportion of melt and crystals) of AMCs are not static and change on the time scale of eruptive cycles (years to centuries) (Wilcock & Delaney, 1996; Singh *et al.*, 1998).

It is well known from ophiolite studies that the roofs of AMCs can be marked by polyphase magmatism and intense interactions between hydrothermal fluids and rocks, particularly within the uppermost few hundred metres of the gabbros (e.g. Pallister & Hopson, 1981; Rothery, 1983; Pedersen, 1986; Nicolas & Boudier, 1991). A distinctive feature of ophiolitic upper gabbros is the presence of leucocratic lithologies (collectively called plagiogranites) in vein networks and/or discrete bodies that commonly contain partially resorbed xenoliths of basaltic material. These lithologies are attributed to partial melting of basaltic material, extreme fractional crystallization of basaltic melt, or a combination of these two end-members (Pedersen & Malpas, 1984). A less well-known feature of ophiolites is the presence of very fine-grained hornfelsic

*Corresponding author. Telephone: 1-250-472-4023. Fax: 1-250-721-6200. E-mail: kgillis@uvic.ca

rocks that occur within narrow contact aureoles centred at the sheeted dyke–gabbro transition (Beard, 1990; Gillis & Roberts, 1999) and as patches within the upper gabbros (Boudier *et al.*, 2000). These hornfelses contain leucocratic material that could result from either the injection of felsic melt into the hornfels or segregation of a melt that was derived by partial melting of the hornfels (Beard, 1990). Studies of mafic contact aureoles show that partial melting is a common process in continental settings (Nasland, 1986; Pattison & Harte, 1988) but the formation of anatectic migmatites has not hitherto been rigorously examined for an oceanic spreading centre.

The aim of this study is to document the most complete and compelling evidence for partial melting within the roof of an AMC, as exposed in the Troodos ophiolite, Cyprus. Field relationships, whole-rock geochemistry, amphibole trace element chemistry, thermometry, mineral textures, and trace element melting models indicate that associated high-grade hornfels and leucocratic rocks are best interpreted as anatectic migmatites. It is shown that short-lived thermal excursions, caused by magmatic intrusion into the base of the sheeted dyke complex, lead to heterogeneous partial melting (0 to >30%) and melt segregation within the overlying conductive boundary layer. We hypothesize that partial melting is a common process within AMC roofs and that a component of geophysically imaged AMCs at fast-spreading ridges may, at times, be partially melted upper crust rather than partially crystallized magma. We also speculate that assimilation of anhydrous hornfels and hydrous leucocratic melt, the products of partial melting, by AMCs is likely to be an important process at fast-spreading MORs.

GEOLOGICAL BACKGROUND

The Troodos ophiolite, Cyprus, is Turonian in age (Blome & Irwin, 1985; Mukasa & Ludden, 1987) and formed in a suprasubduction zone setting within the Tethys Ocean (Miyashiro, 1973; Pearce *et al.*, 1984). Field relationships suggest that magmatism generally kept pace with spreading with only brief periods of amagmatic extension (Varga & Moores, 1990). Because most or all of the amagmatic extension developed off-axis (e.g. van Everdingen & Cawood, 1995; Varga *et al.*, 1999), it did not significantly influence axial processes. A sharp volcanic to sheeted dyke transition, the absence of significant plastic deformation in the gabbros, and the subdued topography along the volcanic–sediment boundary suggest intermediate to fast rates of spreading (Varga & Moores, 1990).

The sheeted dyke–plutonic transition is well exposed to the east of Mount Olympus. Here, the base of the sheeted dyke complex is most commonly intruded by a gabbronorite sequence (Malpas & Brace, 1987). It is separated from the plutonic sequence by a thin (10–30 m thick) contact aureole (Gillis & Roberts, 1999). Horizontally layered gabbros or non-layered gabbros extend up to the base of the sheeted dykes and are infiltrated by leucocratic vein networks. Within the uppermost 100 m of the gabbros, the proportion of leucocratic material systematically increases from <10% to 30% as the contact is approached. The origin of this leucocratic material is not known, because of a high degree of weathering to zeolites and clay minerals. Plagiogranite bodies (<10 m to a few hundred metres in width) locally intrude into the sheeted dyke complex at the same structural level as the contact aureole and have gradational or intrusive boundaries with surrounding gabbros (Malpas & Brace, 1987; Malpas, 1990). The term 'plagiogranite' is used here to describe heterogeneous outcrops composed of amphibole-bearing gabbros, quartz diorites and tonalites. Leucocratic veins and thin dykes within the basal dykes may locally be traced to a discrete plagiogranite body, although in most cases it is not possible to observe this association. Gabbros and plagiogranites commonly contain hornfelsic xenoliths that indicate that the basal sheeted dykes were stoped, recrystallized and partially assimilated into the magmatic system at very high temperatures (e.g. two-pyroxene thermometry yields an average of 1028°C for a hornfels xenolith, K. M. Gillis, unpublished data, 1998).

The contact aureole at the base of the sheeted dyke complex was studied in detail between the villages of Platanistasa, Polystipos and Alona [see fig. 1 of Gillis & Roberts (1999)]. It is composed of pyroxene and hornblende hornfelses cut by an anastamosing leucocratic vein network that gives outcrops a migmatitic appearance. Before the development of the contact aureole, the sheeted dykes were hydrothermally altered at greenschist-facies conditions (Gillis & Roberts, 1999). Magmatic intrusion promoted recrystallization within a thin basal zone (10–30 m) of these dykes at amphibolite- to granulite-facies conditions and local formation of leucocratic vein networks. Gillis & Roberts (1999) proposed that the hornfelsic and leucocratic rocks evolved within a conductive boundary layer that separated an active hydrothermal system from the magmatic heat source that drove it. This boundary is locally cut by mineralized (Cu–Fe sulphides, chlorite, epidote, quartz) faults that were the conduits for moderate-temperature (300–350°C) hydrothermal fluid flow, which suggests that the conductive boundary layer evolved at a spreading centre where vigorous hydrothermal circulation was prevalent (Gillis, 2002).

ANALYTICAL METHODS

Major element mineral compositions were determined using a JEOL JXA-8900R electron microprobe at the

University of Alberta. Instrument calibration was based on natural standards and ZAF corrections were applied to all analyses.

Amphibole trace element contents were analysed at the University of Victoria by laser ablation inductively coupled plasma mass spectrometry (LA-ICP-MS) using thick ($\sim$100 μm) polished sections. A Merchantek Nd:YAG laser, frequency quadrupled to 266 nm, was operated in a gated Q-switched mode for optimum stability. The pulse rate was 5 Hz and the output energy $\sim 70 \pm 10$ mJ, producing cylindrical pits with sharp edges that ranged from 50 to 75 μm in diameter. The ablated material was transported in a flow of argon to a VG PQ II S ICP-MS system. Time-resolved spectra were acquired in peak-jumping mode over a period of 120 s. Background levels of all elements were determined by collecting a 60 s gas blank after which the laser was fired and data were acquired for the remaining 60 s. Sample concentrations were calibrated against duplicate analyses of NIST 613 (Kane, 1998) at the beginning and end of each analytical session (20 analyses). Calcium from electron microprobe analyses was used as the internal standard. A glass standard, prepared from the US Geological Survey reference material BCR-2 (basalt) according to the method outlined by Chen (1999), was also analysed as an unknown at the beginning and end of each analytical session. Relative standard deviations, calculated from repeat analyses of BCR-2, are less than 6% for all elements (see Table 1 below).

Whole-rock major element and Zr compositions were determined by X-ray fluorescence at the Cominco Ltd. laboratory (Vancouver, Canada). Trace elements were analysed by ICP-MS at Cardiff University using Rh as the internal standard for Rb, Sr, Y and Nb, and Re for the rare earth elements (REE), Cs and Ba. Secondary drift was monitored by analysing a standard after every five samples. Mafic rocks were dissolved using a HF–HNO_3 dissolution procedure whereas leucocratic rocks were digested following fusion with a Li-metaborate flux. Mafic samples that were dissolved by both methods have trace element contents that are within 10%.

MIGMATIZED CONTACT AUREOLE

In this section, the field, petrographic and geochemical characteristics of the lithologies that make up the contact aureole are presented.

Nomenclature

An extensive series of descriptive and interpretative terms are used to describe the lithologic and structural components of migmatites (e.g. Sawyer, 1999). Here, we follow a simple nomenclature commonly applied in the study of anatectic migmatites: (1) the mesosome (basal sheeted dykes) represents the protolith of the migmatized contact aureole; (2) the melanosome (mafic hornfels) is the restite or melting residue that may contain trapped melt; (3) the leucosome is the leucocratic melt produced by partial melting of the mesosome. 'Trapped melt' is used here as a general term to describe melt that was generated by partial melting of a mesosome that has crystallized within the matrix of a melanosome.

Outcrop features

The migmatized contact aureole occurs as massive outcrops. Chilled dyke margins are rare and commonly sinuous, and dyke orientations are more variable than in the main sheeted dyke complex (Gillis, 2002). There is no evidence of crystal plastic deformation within the contact aureole or associated sheeted dyke and gabbroic complexes.

The contact aureole is composed of very fine-grained mafic hornfels and slightly coarser-grained tonalitic material, which are interpreted as melanosome and leucosome domains, respectively. Leucosomes are most common within the 10 m closest to the gabbros, where they compose up to 15% of the outcrops. They have a variety of forms that are described here as veins, pockets, patches and zones. Sharp-sided planar to anastomosing veins (millimetres to a few centimetres in width) appear to be injected into the melanosome (Fig. 1a) but cannot be traced into either the subjacent gabbroic units or overlying sheeted dyke complex. Some veins can be traced for a metre or more across an outcrop whereas others are discontinuous and pinch out. Locally, these veins have diffuse contacts and grade smoothly into the host melanosomes. Millimetre-scale pockets of plagioclase + quartz (Fig. 1b and 1c) and centimetre-size patches of plagioclase + quartz + amphibole (Fig. 1c) are locally disseminated within the melanosome matrix over distances of tens of centimetres. They may grade into veins with diffuse contacts but are most commonly cut by sharp-sided veins (Fig. 1b). In two of the studied localities, decimetre-wide leucocratic vein networks form up to 30% of the outcrops over a distance of 10–20 m (Fig. 1d). These are equivocal features because angular fragments of hornfels cut by leucosome veins resemble xenoliths hosted in plagiogranite bodies (Malpas, 1990). On a two-dimensional surface, however, these leucosome veins do not appear to be connected to a plagiogranite body hosted within the gabbro sequence or sheeted dyke complex. Therefore, this type of leucosome is hereafter called a 'leucosome zone', to distinguish it from centimetre-size leucosome veins.

Table 1: Major (wt %) and trace (ppm) element contents of amphibole

Sample:	KG9947	KG9947	KG9947	KG9964	KG9964	KG9948	KG9950	KG9950	KG9950	KG9950	KG9950	KG9950	KG9978	KG9978	KG9946	KG9946	KG9948	KG9948	KG9948	KG9964
Lith:	melan. HH	melan. HH	melan. HH	melan. PH	melan. PH	melan. PH	melan. PH	melan. PH	melan. PH	melan. PH	melan. PH	melan. PH	melan. PH	melan. PH	leuco. vein	leuco. vein	leuco. vein	leuco. vein	leuco. vein	leuco. vein
SiO_2	49·18	49·18	49·26	50·82	50·82	49·26	48·14	48·10	46·90	48·08	47·68	48·12	48·81	47·78	48·00	48·00	49·25	48·94		48·60
TiO_2	1·25	1·25	1·05	0·91	0·91	1·05	1·22	1·36	1·49	1·30	1·30	1·31	1·21	1·48	1·26	1·26	1·25	1·33		1·31
Al_2O_3	5·54	5·54	5·50	4·55	4·55	5·50	6·04	6·03	6·85	6·18	6·14	6·03	5·90	5·69	6·33	6·33	5·65	5·81		6·19
Cr_2O_3	—	—	—	0·04	0·04	—	0·01	—	0·02	0·02	—	0·02	0·02	0·01	—	—	—	—		0·04
FeO	13·35	13·35	12·99	11·94	11·94	12·99	12·81	12·69	13·12	12·69	12·71	12·68	13·98	12·83	13·47	13·47	13·23	12·93		12·37
MgO	15·41	15·41	16·18	16·54	16·54	16·18	15·92	15·86	15·43	15·99	15·52	15·74	14·95	15·95	15·28	15·28	16·18	15·64		15·79
MnO	0·14	0·14	0·13	0·17	0·17	0·13	0·19	0·18	0·21	0·16	0·18	0·20	0·22	0·18	0·23	0·23	0·17	0·13		0·19
CaO	11·08	11·08	10·39	11·31	11·31	10·39	10·46	10·53	10·38	10·30	10·77	10·69	11·03	10·60	10·90	10·90	10·51	10·91		10·80
Na_2O	1·14	1·14	1·22	0·70	0·70	1·22	1·42	1·43	1·66	1·44	1·45	1·42	1·00	1·24	1·22	1·22	1·21	1·20		1·46
K_2O	0·13	0·13	0·12	0·13	0·13	0·12	0·12	0·11	0·11	0·08	0·16	0·11	0·22	0·24	0·12	0·12	0·11	0·12		0·12
F	0·05	0·05	0·11	0·04	0·04	0·11	0·48	0·44	0·49	0·37	0·45	0·38	0·04	0·19	0·08	0·08	0·22	0·18		0·44
Cl	0·20	0·20	0·20	0·06	0·06	0·20	0·14	0·15	0·18	0·17	0·17	0·23	0·18	0·16	0·29	0·29	0·23	0·22		0·17
Total	97·48	97·48	97·15	97·21	97·21	97·15	96·93	96·89	96·83	96·79	96·51	96·92	97·57	96·34	97·17	97·17	98·00	97·41		97·48
Sr	12·6	7·67	7·7	6·62	23·8	28·9	8·16	17·9	11·7	8·97	—	18·3	8·85	10·2	7·82	9·87	10·2	5·78	7·54	11·2
Y	266	156	186	21·2	26·7	178	507	512	430	339	330	334	20·7	96·8	482	402	424	189	218	432
Zr	89·5	50·3	55·3	17·3	21·6	85·2	131	125	152	119	79·4	114	19·6	54·1	59·6	44·1	57·1	49·4	41·2	109
La	4·52	3·94	3·89	0·57	1·01	2·62	8·14	7·59	6·30	5·63	7·74	7·40	0·83	4·11	4·88	7·62	5·44	4·84	3·89	5·06
Ce	26·8	18·9	21·4	2·18	3·41	16·4	38·9	42·3	34·5	26·3	33·7	32·8	4·03	17·0	25·7	33·6	27·3	20·7	19·0	28·3
Pr	7·32	4·67	4·63	0·46	0·70	4·22	10·8	10·9	9·23	7·27	8·81	8·10	0·66	4·49	7·47	7·87	6·76	4·78	4·26	8·07
Nd	46·5	27·4	31·7	3·39	5·09	34·7	70·3	73·9	67·2	49·4	53·5	52·7	3·13	23·3	52·0	48·7	44·7	27·0	25·9	65·0
Sm	23·4	12·9	14·1	1·25	2·37	12·9	34·5	34·8	26·7	25·4	24·4	24·0	—	6·59	26·5	22·7	20·4	11·3	10·3	32·3
Eu	3·10	2·68	2·23	0·34	0·67	2·03	4·04	3·79	2·90	1·83	2·21	2·04	—	2·48	2·78	2·45	2·68	1·72	1·27	2·91
Gd	30·0	16·0	20·1	2·26	3·55	22·5	53·4	50·5	49·4	36·0	32·9	34·2	3·09	9·25	48·3	39·0	31·3	18·3	15·6	49·7
Tb	5·91	3·12	3·78	0·51	0·60	4·20	9·96	10·7	9·40	7·12	6·53	7·08	0·44	2·11	9·95	7·84	6·71	3·14	3·24	10·6
Dy	41·6	23·1	25·6	3·35	3·96	27·9	77·6	69·7	65·6	48·5	47·7	47·6	2·63	15·4	70·2	53·8	49·6	23·1	24·8	76·5
Ho	9·32	4·95	6·42	0·83	0·95	6·24	16·8	16·3	14·0	11·4	10·8	10·5	0·88	3·41	16·0	11·7	11·2	5·41	6·61	16·2
Er	26·0	15·9	18·3	2·54	2·98	19·4	52·7	48·1	41·2	32·9	34·1	30·7	2·75	10·3	48·8	35·3	41·1	19·5	22·5	43·3
Tm	3·56	2·43	2·90	0·33	0·39	2·44	6·39	7·06	5·63	4·42	4·95	4·29	0·53	1·69	6·82	5·39	6·22	3·07	3·27	6·29
Yb	21·5	14·8	16·5	2·84	3·35	17·8	43·7	40·4	35·1	26·3	29·2	29·6	3·92	8·50	44·7	35·1	42·3	20·6	24·2	34·2
Lu	3·37	2·23	2·53	0·42	0·40	2·82	6·17	5·18	4·58	3·48	4·10	4·37	0·87	1·77	6·32	5·06	7·12	3·37	3·77	5·03

Sample:	KG9964	KG9964	KG9964	KG9964	KG9964	KG9978	KG9978	KG9978	KG9955	KG9974	KG9974	KG9974	KG9944	KG9944	KG9944	KG9944	KG9944	KG9944	BCR-2*		
Lith:	leuco. HH	leuco. vein	leuco. vein	leuco. vein	leuco. vein	leuco. vein	leuco. vein	leuco. vein	leuco. vein	leuco. zone	leuco. patch	leuco. patch	plagio. patch	plagio.	plagio.	plagio.	plagio.	plagio.	Av.	SD	d.l.
SiO_2	48·60	47·84	48·62	48·29	48·51	47·58	47·99	49·06	47·52	48·61	48·73	48·56	45·87	47·34	45·60	45·60	46·14	46·26			
TiO_2	1·31	1·39	1·36	1·38	1·34	1·68	1·26	1·04	0·98	1·19	0·89	1·10	0·83	0·50	0·96	0·96	0·85	0·87			
Al_2O_3	6·19	6·50	6·24	6·54	6·17	6·30	6·20	5·46	4·31	5·81	5·64	5·95	5·90	4·63	6·19	6·19	6·38	5·68			
Cr_2O_3	0·04	—	0·03	0·02	0·03	—	—	—	0·02	0·02	—	0·03	—	—	—	—	—	—			
FeO	12·37	12·57	12·97	12·73	12·45	13·27	13·34	13·04	24·45	13·43	16·43	14·83	26·24	26·24	25·40	25·40	25·39	25·46			
MgO	15·79	15·72	15·77	15·81	15·91	15·60	15·56	15·54	7·91	15·34	13·47	14·54	6·99	7·77	7·48	7·48	7·57	7·99			
MnO	0·19	0·21	0·23	0·17	0·20	0·19	0·17	0·17	0·28	0·17	0·24	0·21	0·58	0·71	0·50	0·50	0·54	0·56			
CaO	10·80	10·80	10·72	10·89	10·87	10·76	10·91	11·17	10·44	10·91	11·19	10·82	10·47	9·44	10·26	10·26	10·20	9·51			
Na_2O	1·46	1·61	1·49	1·58	1·48	1·56	1·26	1·02	1·01	1·18	0·94	1·08	1·19	0·93	1·18	1·18	1·05	1·20			
K_2O	0·12	0·12	0·15	0·14	0·12	0·23	0·27	0·25	0·38	0·19	0·13	0·13	0·51	0·32	0·54	0·54	0·53	0·49			
F	0·44	0·50	0·48	0·42	0·45	0·68	0·26	0·09	0·03	0·25	—	0·08	0·01	0·03	0·01	0·01	—	0·01			
Cl	0·17	0·19	0·19	0·17	0·20	0·21	0·18	0·22	0·31	0·24	0·30	0·25	0·49	0·32	0·43	0·43	0·35	0·38			
Total	97·48	97·45	98·22	98·14	97·72	98·06	97·40	97·06	97·64	97·32	97·96	97·56	99·06	98·23	98·55	98·55	99·00	98·40			
Sr	6·18	11·1	5·86	7·25	7·18	24·5	6·45	9·02	30·3	13·8	14·3	10·2	14·6	14·7	9·42	13·1	9·13	6·25	336	11·2	0·75
Y	349	344	368	394	342	680	403	321	222	54·9	49·2	65·7	99·6	129	141	60·9	95·5	171	34·6	1·96	0·34
Zr	57·8	105	86·7	88·4	82·6	146	92·8	75·9	230	30·3	37·3	26·2	37·9	39·5	53·9	25·2	34·9	80·0	182	12·4	1·07
La	4·6	3·74	4·18	4·26	3·38	11·6	11·9	15·6	6·73	3·92	3·08	1·96	1·92	2·15	3·45	1·36	1·99	4·88	26·2	2·22	0·09
Ce	26·1	18·5	24·1	21·7	18·1	57·3	57·4	65·3	25·5	13·8	8·21	5·57	5·76	6·91	9·82	4·29	7·03	16·7	49·1	3·27	0·05
Pr	7·48	5·88	7·17	6·90	5·21	17·0	15·5	15·2	5·59	2·44	1·63	1·51	1·24	1·45	2·16	0·79	1·47	3·32	6·64	0·52	0·05
Nd	56·2	47·0	53·0	47·9	39·9	126	102	88·4	35·6	12·5	7·90	8·36	8·64	10·4	13·3	5·35	9·88	21·4	28·9	2·26	0·20
Sm	29·2	25·2	28·0	23·5	22·0	63·2	39·4	30·4	13·3	5·33	—	4·70	4·56	5·00	7·98	3·07	4·63	9·27	7·01	0·84	0·31
Eu	2·55	1·51	2·97	3·03	2·27	3·60	3·38	1·70	1·07	0·86	—	—	0·61	0·50	0·66	0·47	0·39	0·69	1·95	0·18	0·15
Gd	43·6	40·9	39·8	42·2	37·9	97·4	55·9	42·6	19·3	6·66	6·32	4·39	9·29	9·96	13·8	5·08	8·79	17·0	6·42	0·54	0·32
Tb	8·80	7·74	8·53	8·63	7·66	19·2	10·3	7·59	3·70	1·11	1·09	1·49	2·19	2·40	2·81	1·14	2·14	3·48	1·06	0·07	0·06
Dy	59·6	55·9	56·8	59·1	53·7	124	69·9	51·0	28·5	7·62	7·96	9·18	14·3	17·9	20·5	9·57	14·3	24·8	6·52	0·80	0·20
Ho	12·5	11·5	12·2	13·2	11·7	27·6	16·3	11·0	6·13	1·87	1·71	2·65	3·47	4·12	4·79	1·96	3·13	5·54	1·31	0·15	0·05
Er	37·5	38·1	37·5	36·3	33·7	84·0	41·3	34·6	20·4	5·67	5·59	6·94	10·4	13·7	15·5	6·40	10·6	18·0	3·92	0·47	0·20
Tm	5·11	4·83	5·75	5·01	4·12	10·3	6·35	4·60	2·98	0·75	0·78	0·93	1·74	2·07	2·22	0·92	1·66	2·37	0·59	0·10	0·05
Yb	29·4	26·4	29·9	29·3	25·1	56·1	41·8	33·7	20·3	6·34	5·19	5·97	12·1	13·5	14·0	7·23	10·3	16·2	3·49	0·44	0·20
Lu	3·96	4·00	4·25	3·95	3·18	8·04	4·88	4·95	2·99	0·86	0·62	0·94	1·76	2·17	2·39	1·18	1·68	2·38	0·54	0·07	0·05

*Average, standard deviation and detection limits for glass standard BCR-2 run during analytical sessions ($n = 6$).
—, below detection limit; melan., melanosome; leuco., leucosome; HH, hornblende hornfels; PH, pyroxene hornfels; plagio., plagiogranite.

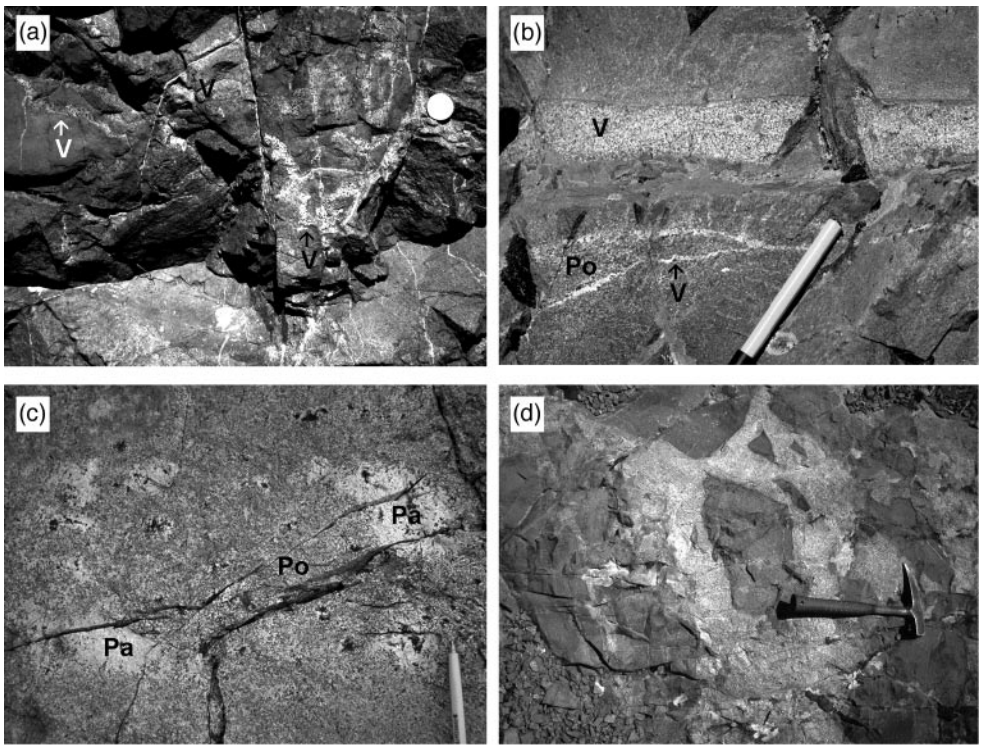

Fig. 1. Outcrop photographs of the contact aureole showing the distribution of leucocratic and mafic rock types. (a) Hornfels cut by leucocratic veins (scale: coin is 2 cm in diameter). (b) Millimetre-scale leucocratic pockets associated with leucocratic veins within hornfels (scale: pen is 14 cm long). (c) Millimetre-scale leucocratic pockets and centimetre-scale leucocratic patches not associated with leucocratic veins (scale: pen is 10 cm long). (d) Decimetre-scale leucocratic zone within pyroxene hornfels (scale: hammer is 25 cm long). Po, pockets; Pa, patches; V, vein.

Petrographic features

The mesosome (basal sheeted dykes above the contact aureole) is pervasively altered to greenschist- and amphibolite-facies mineral assemblages (Gillis & Roberts, 1999). Clinopyroxene is completely replaced by fibrous to granular amphibole + secondary magnetite, plagioclase is partially albitized, and interstitial zones are composed of amphibole ± quartz ± chlorite ± epidote ± titanite. Where present, chlorite and quartz are minor phases (<5 modal %) and epidote occurs in trace amounts.

The melanosome is composed of pyroxene and hornblende hornfelses (Gillis & Roberts, 1999). Where both types of hornfels have been identified at the same outcrop, the hornblende hornfelses are adjacent to the basal dykes and the pyroxene hornfelses are closest to the gabbros. Both types have a broad range in textures that are indicative of both solid-state recrystallization and partial melting.

Pyroxene hornfelses have been completely recrystallized at granulite-facies conditions and are composed of zoned plagioclase (cores $An_{53–87}$; rims $An_{42–82}$) (50–55%), clinopyroxene (20–30%), orthopyroxene (2–6%), ilmenite and magnetite (total oxides 1–3%), ± quartz (up to 15%), ± amphibole (up to 10%). Samples have either a uniform or bimodal grain size and display two common textures. The first resembles the diabasic textures common to the sheeted dykes. What is different from the dykes is that aggregates of very fine-grained (<0·02–0·15 mm) granular clinopyroxene, orthopyroxene, magnetite, and ilmenite are interstitial to fine-grained (0·2–1 mm) acicular plagioclase (Fig. 2a). The shape and size of the pyroxene and Fe–Ti oxide aggregates mimic those of the fibrous amphibole clusters that pseudomorph clinopyroxene in the main sheeted dyke complex. This suggests an origin through prograde metamorphism of hydrothermally altered dykes (Gillis & Roberts, 1999). Plagioclase has straight or irregular grain boundaries that are locally lined with very fine-grained granoblastic plagioclase and/or clinopyroxene (Fig. 2a). Very fine-grained inclusions of rounded clinopyroxene occur within the outer margin of some plagioclase crystals. The second common texture is very fine-grained with granoblastic plagioclase, clinopyroxene, orthopyroxene, and Fe–Ti oxides (Fig. 2b and d), typical of texturally equilibrated mafic granulites. Many samples display both textures, with either sharp or gradational boundaries between fine-grained and very fine-grained zones. In some samples these boundaries are curved or swirling and in others plagioclase laths are aligned over intervals of several millimetres and are suggestive of a magmatic

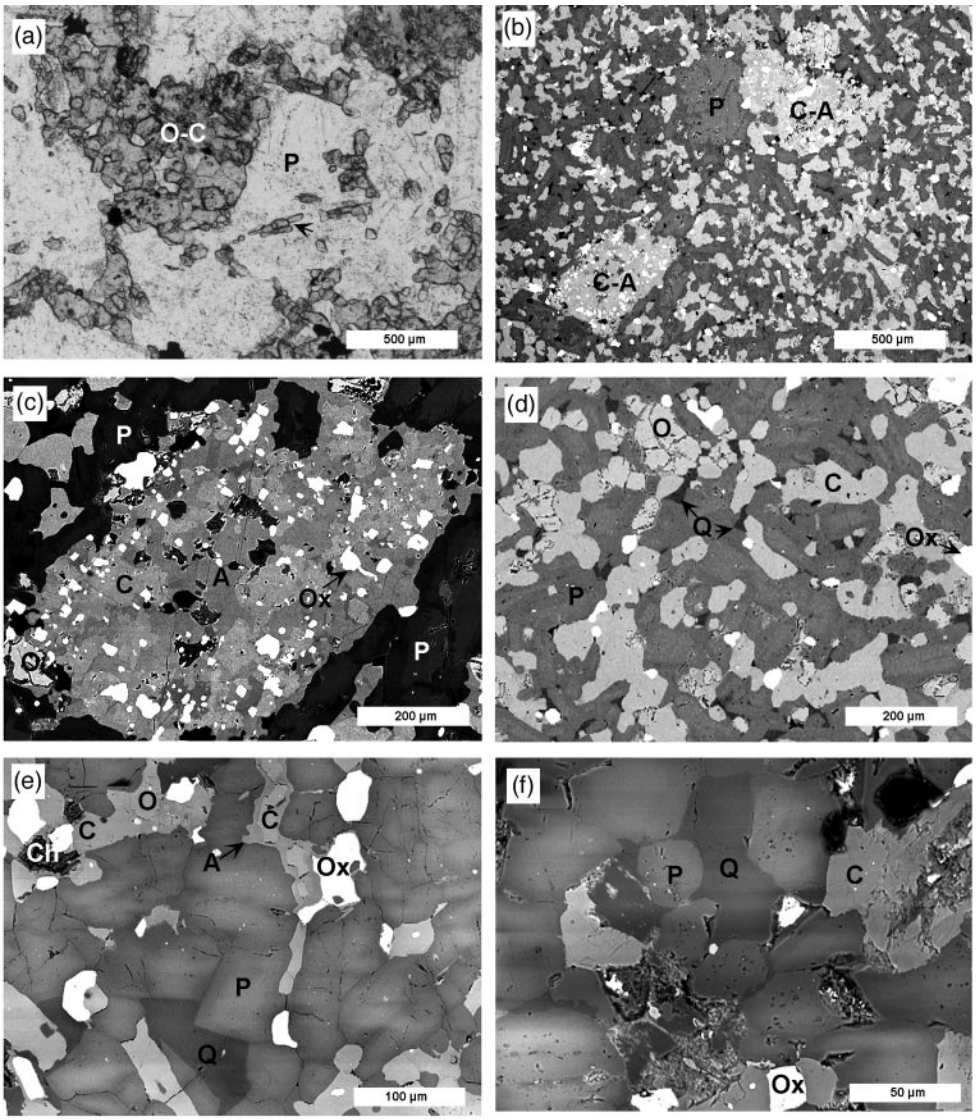

Fig. 2. Images showing typical textures in the pyroxene hornfels. (a) Photomicrograph showing very fine-grained, granular aggregates of orthopyroxene and clinopyroxene and fine-grained plagioclase; the arrow points to a plagioclase margin rimmed with granular pyroxene (sample KG9356). (b) Scanning electron microscope (SEM) image of very fine-grained granular groundmass of clinopyroxene, orthopyroxene, plagioclase, and Fe–Ti oxides with relict plagioclase and pyroxene aggregates (sample KG9292). (c) Enlargement of SEM image shown in (b) (lower left corner) with a relict mafic cluster where brown granular amphibole mantles pyroxene (sample KG9292). (d) SEM image showing very fine-grained, granoblastic pyroxene hornfels (sample KG9292). (e) SEM image showing a quartz pocket in contact with faceted plagioclase grains; orthopyroxene is locally replaced by chlorite whereas the other phases are unaltered; brown granular amphibole mantles clinopyroxene (sample KG9948). (f) SEM image showing a quartz pocket in contact with rounded plagioclase grains (sample KG9948). Abbreviations: C, clinopyroxene; P, plagioclase; O, orthopyroxene; Q, quartz; Ox, Fe–Ti oxide; A, amphibole; Ch, chlorite.

flow fabric (e.g. Nicolas, 1992). In most samples, brown, granular amphibole rims isolated grains or aggregates of pyroxene (Fig. 2c and e) and forms grains that are interstitial to plagioclase.

The hornblende hornfelses have been mostly (>75%) to completely recrystallized at amphibolite-facies conditions (Gillis & Roberts, 1999). They are composed of plagioclase (45–55%), amphibole (10–20%), clinopyroxene (20–40%), Fe–Ti oxides (1–3%), ± quartz (up to 5%), ± titanite. They are similar to the pyroxene hornfelses with the following exceptions: (1) they lack orthopyroxene; (2) most hornblende hornfelses have a bimodal grain size and none have a uniform, very fine-grained, granoblastic texture; (3) plagioclase is slightly less calcic (cores $An_{51–69}$; rims $An_{37–57}$); (4) brown granular amphibole locally rims cores of fibrous green amphibole.

Leucosomes are typically coarser grained than associated melanosomes and have a wide range in modal

mineralogy. Leucosome veins are composed of plagioclase (cores $An_{41–82}$; rims $An_{29–65}$) and quartz in approximately equal proportions, with minor brown granular amphibole (<5%) and trace clinopyroxene, apatite, zircon and Fe–Ti oxides. Their transition into the host melanosomes is commonly marked by a slight increase in the abundance of brown amphibole. Leucosome pockets are composed of quartz, plagioclase, ± clinopyroxene, ± amphibole. Faceted, and more rarely, rounded grain boundaries are in contact with quartz and are indicative of crystallization from a melt (Fig. 2e and f). Leucosome patches and zones are more mafic than leucosome veins and pockets, with up to 40% amphibole and <10% quartz.

Both types of hornfels show local evidence of retrograde metamorphism. Orthopyroxene is commonly replaced by chlorite ± titanite, even in samples that are otherwise fresh (Fig. 2e). Clinopyroxene and brown granular amphibole may be partially to completely replaced by actinolitic amphibole. Albitic plagioclase and acicular amphibole locally line microfractures in plagioclase. The degree of retrograde metamorphism within the leucosomes is generally higher than in their host hornfels, with plagioclase being the most pervasively altered phase to assemblages of albitic plagioclase, chlorite and epidote.

Whole-rock chemistry

The major and trace element compositions of the melanosome hornfelses; leucosome veins, patches and zones; and plagiogranites hosted within the gabbroic sequence are given in Table 2. Leucosome pockets could not be separated from their host rock because of their small size and irregular shape. The melanosome hornfelses show only minor compositional shifts from the average mesosome dyke but have slightly lower SiO_2, and higher Al_2O_3 and CaO contents (Fig. 3). Pyroxene hornfelses also have slightly lower Fe_2O_3 and higher MgO than the average mesosome dyke (Fig. 3). Relative to chondritic values, all melanosomes are light rare earth element (LREE) depleted [$(La/Sm)_N = 0·39–0·62$] (Fig. 4a and b). Relative to the average mesosome dyke, the melanosome hornfelses show enrichment and depletion in both their total REE and LREE contents, with flat to slightly enriched Eu (Fig. 4d and e).

Leucocratic veins, patches and zones range in composition from quartz diorite to tonalite, and are enriched in SiO_2 and depleted in Al_2O_3, Fe_2O_3, MgO and CaO relative to the melanosome hornfelses and mesosome dykes (Fig. 3). They show chemical trends that can be explained by either partial crystallization and/or partial melting. For example, progressive melting at low-pressure, hydrous conditions of a metabasaltic protolith leads to a decrease in SiO_2 and increase in Al_2O_3 in the melts produced (e.g. Beard & Lofgren, 1991) (Fig. 3) whereas plagioclase-dominated crystallization produces the opposite trends. Their REE patterns are distinctive from the other lithologies (Fig. 4c) in that leucosome veins have higher $(La/Sm)_N$ (0·57–0·95), flat heavy REE (HREE), and negative Eu anomalies despite the high modal plagioclase contents. The leucosome patch and zones have slightly lower $(La/Sm)_N$ ratios (0·36–0·41) and small negative or positive Eu anomalies. Relative to the average mesosome dyke, leucosome veins are enriched in total REE and LREE, with a few samples showing HREE depletion, whereas the leucosome patch and zones show only minor differences (Fig. 4f).

Plagiogranites have lower Fe_2O_3 and higher Al_2O_3 contents (Fig. 3), and lower total REE contents than the leucosomes. Their chondrite-normalized $(La/Sm)_N$ ratios are comparable with those of the leucosome zones but lower than those of leucosome veins and patches (compare Figs 4c and 5). Plagiogranites from other areas in the Troodos ophiolite (Aldiss, 1978; J. Ludden, unpublished data, 1987) display a much broader range in composition than those reported here, reflecting the extreme lithological heterogeneity evident in the field (Fig. 5). Because of these complexities, detailed examination of the link between the leucocratic melts generated within the contact aureole and plagiogranites is beyond the scope of this study.

Amphibole chemistry

The major and trace element contents were determined for amphiboles hosted within leucosome veins, melanosome hornfelses and plagiogranites (Table 1). The majority of the analysed grains are brown granular hornblende with TiO_2 and Al_2O_3 contents greater than 1 and 4·5 wt %, respectively. These occur as rims on (Fig. 2e), and intergrowths with (Fig. 2c), pyroxene in the melanosome hornfelses and as isolated grains in the leucosome veins. Compositional data were also obtained for a few grains of fibrous, actinolitic amphibole that pseudomorphically replace pyroxene. Plagioclase–amphibole thermometry yields high equilibration temperatures for brown granular hornblende hosted by both rock types (melanosome hornfels: average 805°C, $n = 40$; leucosome veins: average 770°C, $n = 35$); lower temperatures were recorded for actinolitic amphibole (Fig. 6).

All amphiboles are LREE depleted with approximately flat HREE and negative Eu anomalies (Fig. 7). Granular brown hornblende has significantly higher total REE contents and is more LREE depleted relative to the host lithology (Fig. 7a). Hornblendes hosted in hornblende hornfels have slightly lower REE concentrations than those in the pyroxene hornfels (Fig. 7a). Amphiboles in

Table 2: Major (wt %) and trace (ppm) element contents of whole rocks

Sample:	KG9945	KG9356A	KG93125	KG93215	KG9965B	KG9947	KG9292	KG9256	KG9379	KG93171	KG93181	KG9948	KG9950	KG9953A	KG9964A
Lith.:	gabbro	melan. HH	melan. HH	melan. HH	melan. HH	melan. HH	melan. PH	melan. PH	melan. PH	melan. PH	melan. PH	melan. PH	melan. PH	melan. PH	melan. PH
SiO_2	49·04	53·77	53·54	53·61	51·68	54·49	52·00	54·86	47·90	54·45	50·22	50·27	55·04	53·49	50·24
TiO_2	1·36	1·55	0·58	1·46	0·47	1·26	0·88	1·00	1·18	0·61	0·62	1·38	0·82	0·77	0·60
Al_2O_3	15·43	14·63	16·80	14·92	15·30	15·22	15·25	15·32	16·95	15·17	15·69	15·26	15·14	15·51	15·68
Fe_2O_3	15·97	12·02	7·59	12·00	9·77	9·92	9·34	10·39	11·97	9·77	9·10	12·89	9·61	10·59	9·13
MnO	0·20	0·05	0·10	0·09	0·12	0·07	0·10	0·10	0·18	0·14	0·12	0·07	0·10	0·12	0·15
MgO	4·53	4·42	6·01	4·64	7·19	5·11	6·65	4·82	7·18	6·44	8·21	5·25	5·17	5·57	8·93
CaO	8·81	9·75	11·53	9·87	11·06	9·22	11·76	10·31	12·66	11·63	13·17	10·51	9·93	10·27	12·43
Na_2O	1·84	2·57	1·97	2·16	2·15	3·03	2·80	2·39	1·95	1·08	1·53	3·35	2·15	2·15	1·40
K_2O	0·28	0·05	0·11	0·04	0·07	0·09	0·03	0·01	0·00	0·02	0·01	0·02	0·10	0·03	0·01
P_2O_5	0·03	0·10	0·03	0·11	0·02	0·07	0·07	0·09	0·04	0·05	0·05	0·07	0·07	0·05	0·03
LOI	2·30	0·66	1·39	0·49	1·29	0·92	0·94	0·43	0·29	0·31	0·61	0·25	1·01	0·57	0·70
Total	99·80	99·58	99·66	99·41	99·13	99·41	99·83	99·73	100·32	99·68	99·34	99·33	99·15	99·13	99·31
Rb	—	0·36	0·67	—	0·41	0·17	0·13	0·15	0·66	—	0·09	0·16	0·75	0·65	0·11
Sr	71	129	99	143	77	112	110	113	123	87	95	139	105	68	72
Y	10·3	33·6	22·4	34·3	16·1	26·9	24·7	25·1	21·6	14·9	16·7	27·2	29·6	20·4	16·1
Zr	16	—	—	—	30	71	54	—	—	—	—	—	79	54	35
Nb	1·38	1·04	0·63	1·39	0·52	1·25	0·68	0·88	0·50	3·41	0·38	0·76	1·03	0·69	0·39
Ba	12·8	7·09	8·67	7·43	14·0	11·5	11·2	9·05	7·21	7·16	6·80	8·60	12·7	11·1	5·84
La	0·41	2·62	1·97	2·44	0·82	1·78	1·85	1·69	1·27	0·98	0·80	1·76	2·59	1·40	1·08
Ce	1·12	8·29	5·75	8·72	2·61	6·19	6·25	5·42	4·17	3·02	2·70	5·51	7·89	4·26	3·19
Pr	0·21	1·42	0·98	1·46	0·46	1·03	1·14	0·97	0·69	0·52	0·52	1·00	1·34	0·75	0·56
Nd	1·29	8·40	5·48	8·51	2·82	6·37	6·59	5·93	4·36	3·12	3·20	6·22	7·42	4·38	3·44
Sm	0·60	3·06	2·01	2·87	1·13	2·48	2·43	2·26	1·74	1·29	1·30	2·35	2·61	1·68	1·33
Eu	0·38	1·13	0·93	—	0·57	0·91	0·89	0·93	—	0·54	0·59	1·02	0·82	0·68	0·55
Gd	1·18	4·39	2·87	—	1·74	3·46	3·33	3·21	—	2·12	2·01	3·37	3·64	2·48	1·97
Tb	0·27	0·84	0·57	0·79	0·36	0·59	0·64	0·63	0·50	0·44	0·39	0·68	0·71	0·50	0·39
Dy	1·80	5·42	3·56	5·42	2·45	4·04	4·17	4·04	3·56	2·80	2·55	4·41	4·69	3·24	2·40
Ho	0·43	1·19	0·81	1·21	0·56	0·97	0·91	0·89	0·77	0·59	0·59	0·96	1·02	0·73	0·55
Er	1·33	3·58	2·36	3·39	1·84	2·70	2·69	2·65	2·19	1·83	1·79	2·83	2·99	2·16	1·64
Tm	0·20	0·54	0·36	0·49	0·27	0·47	0·40	0·41	0·31	0·28	0·27	0·43	0·46	0·36	0·25
Yb	1·34	3·35	2·41	3·23	1·83	2·73	2·58	2·70	1·89	1·93	1·73	2·74	3·06	2·19	1·61
Lu	0·20	0·54	0·38	0·47	0·30	0·45	0·41	0·44	0·30	0·31	0·28	0·42	0·48	0·36	0·27

Table 2: continued

Sample:	KG9978B	KG93217	KG9974	KG9946	KG9964B	KG9965A	KG9970	KG9978A	KG9949	KG9953B	KG9954	KG9955	KG9942	KG9941	KG9944
Lith.:	melan. PH	melan. PH	leuco. patch	leuco. vein	leuco. vein	leuco. vein	leuco. vein	leuco. vein	leuco. vein	leuco. zone	leuco. zone	leuco. zone	plagio.	plagio.	plagio.
SiO_2	50·77	51·59	51·86	58·02	72·72	74·08	69·00	67·26	75·25	62·50	69·13	60·77	70·43	71·08	64·92
TiO_2	0·73	1·18	1·49	1·30	0·64	0·47	1·00	0·73	0·33	0·80	0·50	0·79	0·41	0·49	1·11
Al_2O_3	15·75	15·77	13·10	16·02	12·48	12·53	13·00	13·72	11·76	14·81	13·42	14·60	11·64	11·39	11·29
Fe_2O_3	9·55	11·73	14·01	9·72	3·75	3·16	5·44	4·36	2·08	9·09	5·71	8·57	7·71	6·36	10·44
MnO	0·12	0·12	0·09	0·07	0·01	0·01	0·01	0·03	0·01	0·10	0·05	0·14	0·02	0·02	0·11
MgO	7·84	6·08	5·69	2·75	1·37	0·72	1·55	2·72	0·61	1·80	0·91	3·27	0·52	1·08	2·05
CaO	11·77	11·09	8·48	7·09	4·71	4·13	4·03	7·00	4·30	5·13	3·01	5·11	4·25	3·99	5·46
Na_2O	1·79	2·22	2·33	3·22	2·81	3·16	3·27	2·66	3·58	3·51	4·48	3·92	2·70	2·84	1·95
K_2O	0·05	0·02	0·31	0·15	0·09	0·10	0·28	0·07	0·28	0·18	0·30	0·46	0·46	0·43	0·36
P_2O_5	0·05	0·05	0·07	0·25	0·10	0·02	0·20	0·10	0·03	0·17	0·11	0·05	0·09	0·07	0·03
LOI	1·12	0·16	2·16	1·13	0·85	1·23	1·42	0·88	0·99	1·25	1·80	1·99	1·36	1·88	1·84
Total	99·55	100·03	99·60	99·73	99·54	99·62	99·21	99·54	99·23	99·35	99·43	99·68	99·60	99·64	99·55
Rb	0·27	—	0·45	0·27	0·12	0·17	0·38	0·07	1·98	0·25	0·41	0·79	0·63	0·57	0·49
Sr	97	99	128	126	89	130	116	164	146	112	110	95	127	99	80
Y	20·9	19·3	29·6	37·1	21·8	15·9	33·0	35·2	35·0	24·9	34·9	34·6	36·9	35·5	20·8
Zr	48	—	67	95	148	203	109	148	149	45	61	61	46	49	34
Nb	0·59	0·44	1·23	1·98	2·01	1·99	2·42	1·75	1·59	1·24	2·20	1·70	1·91	1·57	1·00
Ba	8·15	8·10	3·56	11·5	14·3	11·3	3·40	11·3	16·7	11·4	13·2	28·6	12·4	8·41	13·6
La	1·54	1·15	2·12	3·69	2·81	2·40	3·79	3·32	3·32	1·59	1·95	1·74	1·55	1·34	0·67
Ce	4·75	4·06	6·65	11·9	8·54	6·98	11·7	10·9	11·0	5·46	6·55	5·60	4·86	5·08	1·91
Pr	0·86	0·65	1·09	1·87	1·22	0·96	1·76	1·78	1·91	0·91	1·07	0·93	0·76	0·87	0·33
Nd	4·88	3·83	6·70	11·0	6·61	5·16	10·35	9·83	10·6	5·91	6·96	5·92	5·03	5·48	2·28
Sm	1·81	1·53	2·45	3·64	2·26	1·58	3·28	3·36	3·66	2·38	2·76	2·37	2·33	2·35	1·02
Eu	0·70	—	0·67	1·06	0·58	0·56	1·02	0·68	1·00	1·14	0·97	0·82	0·75	0·78	0·50
Gd	2·65	—	3·73	5·21	3·10	2·05	4·56	4·79	4·82	3·31	4·37	3·83	3·85	3·81	1·84
Tb	0·52	0·45	0·70	0·88	0·52	0·35	0·78	0·80	0·96	0·63	0·79	0·73	0·77	0·77	0·38
Dy	3·44	3·37	4·48	5·39	3·32	2·37	4·81	5·28	6·04	3·82	5·18	4·76	5·31	5·19	2·75
Ho	0·75	0·73	1·05	1·30	0·76	0·52	1·12	1·16	1·37	0·90	1·25	1·17	1·33	1·26	0·67
Er	2·26	2·14	2·96	3·60	2·16	1·61	3·17	3·45	4·03	2·40	3·52	3·39	3·81	3·54	2·00
Tm	0·34	0·32	0·49	0·61	0·39	0·28	0·52	0·55	0·62	0·39	0·59	0·54	0·65	0·60	0·32
Yb	2·20	2·47	2·99	3·32	2·26	1·79	3·32	3·24	3·90	2·43	3·60	3·36	4·12	3·70	2·00
Lu	0·35	0·30	0·46	0·55	0·38	0·30	0·52	0·52	0·60	0·37	0·60	0·55	0·65	0·61	0·34

—, below detection limit; melan., melanosome; leuco., leucosome; HH, hornblende hornfels; PH, pyroxene hornfels; plagio., plagiogranite.

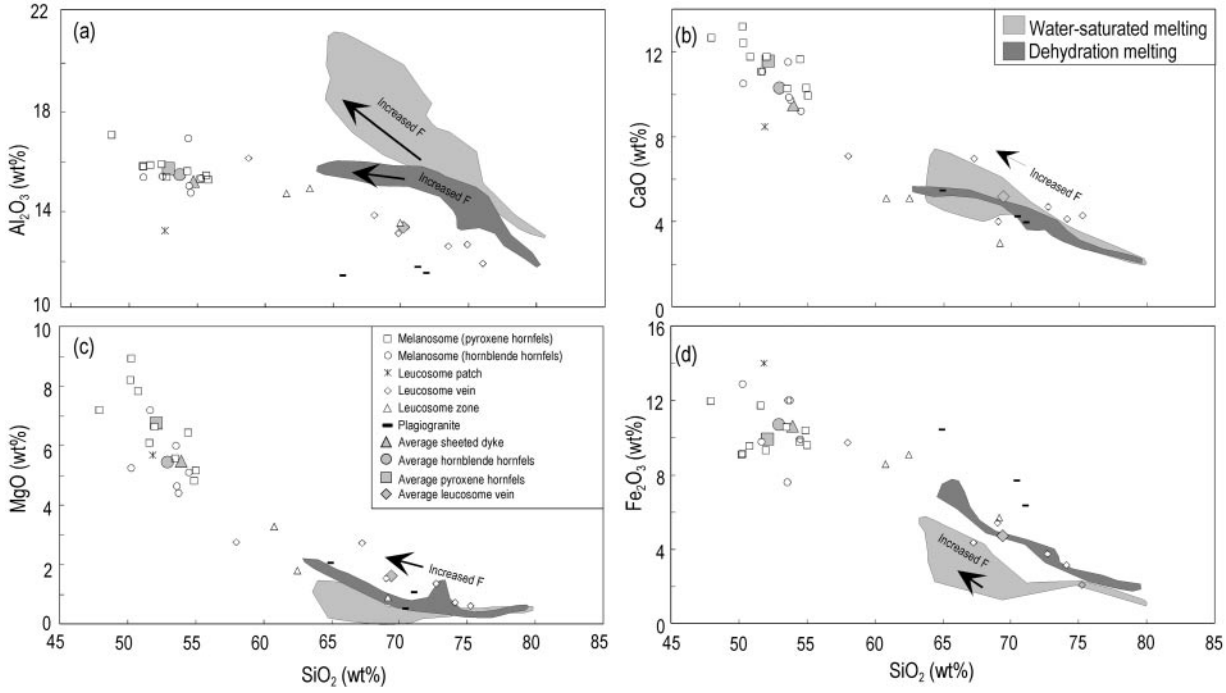

Fig. 3. Whole-rock major element plots. Grey shaded fields show melt compositions produced experimentally by low-pressure (1 kbar), dehydration (dark) and water-saturated (light) partial melting of metabasalt [sample 478 from Beard & Lofgren (1991)], which has a mineralogy very similar to the basal sheeted dykes (see text for additional details).

leucosome patches and zones have REE patterns that are more similar to those of plagiogranites than the leucosome veins (Fig. 7b and c). Amphiboles in plagiogranites have the lowest REE abundances and their LREEs are less depleted than in melanosome hornfels and leucosomes (Fig. 7c).

The composition of the replacive amphibole after clinopyroxene is markedly different from that of the brown granular amphibole and is most similar to that of clinopyroxene (LREE depleted, HREE contents 5–10 times chondritic values; L. Coogan, unpublished data, 1998) and whole-rock values (Fig. 7a). In comparison, brown granular hornblendes hosted in the melanosomes and leucosomes are significantly enriched in the REE relative to clinopyroxene and whole-rock values, and equilibrated at temperatures close to the gabbroic solidus. As there is no doubt that leucosome hornblende crystallized from a magma, we conclude that the most likely origin for melanosome hornblende was by the crystallization of trapped melt.

ANATEXIS WITHIN THE CONTACT AUREOLE

A wide variety of criteria may be used to identify high-grade metamorphic rocks that have been partially melted and to investigate the nature and extent of partial melting (e.g. Sawyer, 1999). In this section, we document microtextural evidence and mineral assemblages that are indicative of preserved trapped melt and melt-producing reactions, respectively. We then use the geochemistry of the melanosomes and leucosomes to examine the nature and extent of partial melting by comparison with experimental studies and development of trace element partial melting models. Field criteria indicative of partial melting have been described above.

Melt textures and melt reactions

Many melanosome samples display textures that are indicative of the crystallization of trapped melt (Sawyer, 1999). Quartz forms triangular to quadrangular pockets (10–200 μm across) at triple junctions between plagioclase ± clinopyroxene ± Fe–Ti oxides (Fig. 2e and f). The interstitial, curvilinear shape of these pockets is typical of melt pockets produced in a variety of partial melting experiments (e.g. Jurewicz & Watson, 1984; Wolf & Wyllie, 1991). Most phases in contact with the quartz pockets have straight grain boundaries (Fig. 2e) indicative of crystallization in the presence of melt (Vernon & Collins, 1988). Rare rounded grains of plagioclase are also in contact with the quartz pockets (Fig. 2f), suggesting

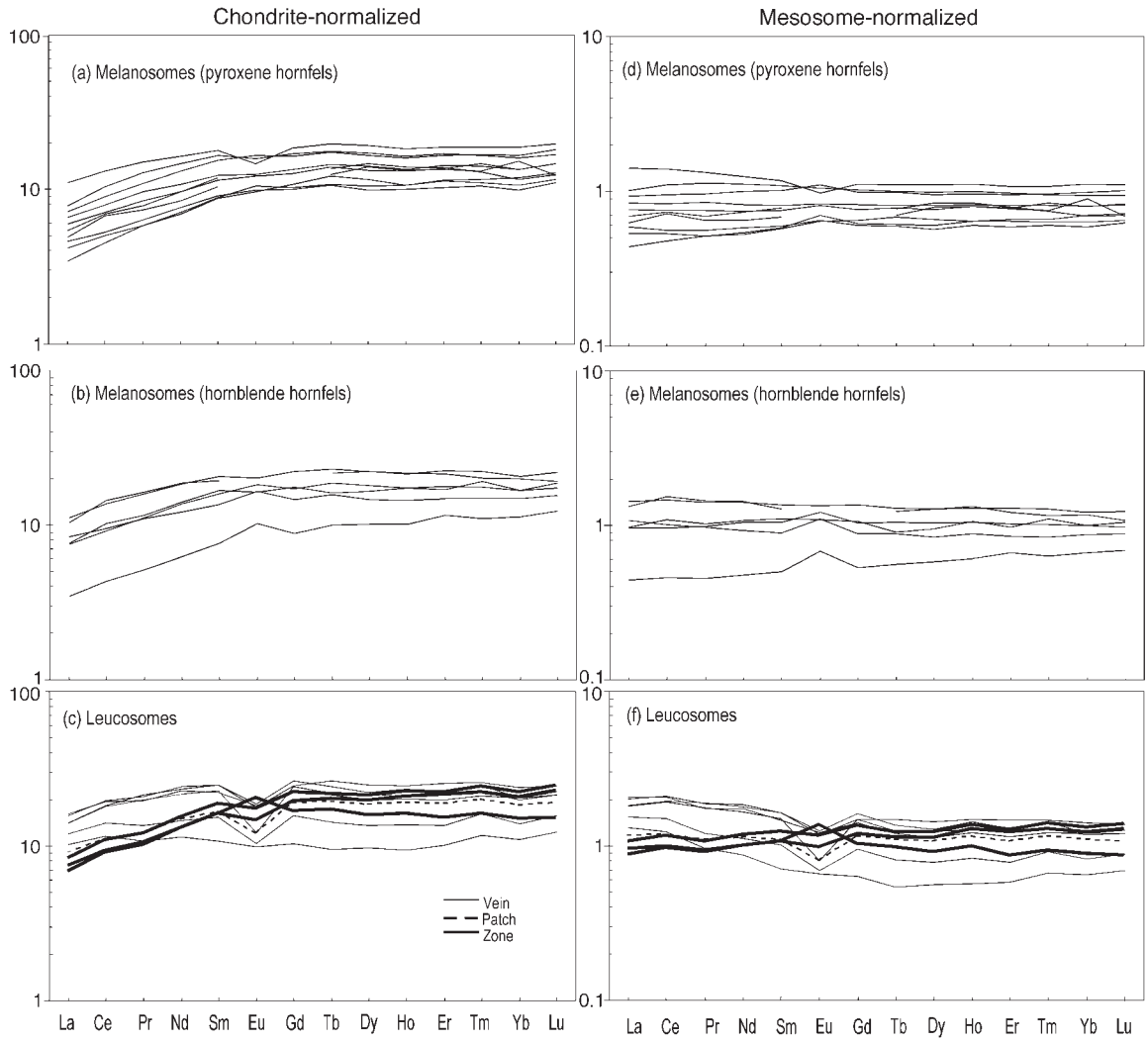

Fig. 4. Chondrite-normalized REE element plots of: (a) melanosome pyroxene hornfels; (b) melanosome hornblende hornfels; (c) leucosome veins, patch and zones [chondritic values from Anders & Grevesse (1989)]. Dyke-normalized REE plots of: (d) melanosome pyroxene hornfels; (e) melanosome hornblende hornfels; (f) leucosome veins, patch, and zones (average dyke from field area, $n = 9$, K. M. Gillis, unpublished data, 1998). Mesosome-normalized values <1 are indicative of partial melting whereas those >1 suggest the presence of trapped melt. Discontinuous lines indicate samples for which Eu and Gd data are not available.

that plagioclase was a reactant in the melting reaction (Busch *et al.*, 1974). The assemblage of quartz + plagioclase ± clinopyroxene ± amphibole ± Fe–Ti oxides within leucosome pockets and patches is also consistent with the crystallization of tonalitic melts, which can be the products of partial melting of amphibolites (e.g. Spulber & Rutherford, 1983; Beard & Lofgren, 1991).

The presence of trapped melt in some samples is also evident from their whole-rock compositions. For example, sample KG9950 contains numerous millimetre-scale or smaller pockets of quartz and plagioclase and is SiO_2 enriched (55 wt %) and LREE enriched relative to the mesosome dykes. On the other hand, sample KG93181, which shows no textural evidence for trapped melt, has lower SiO_2 (50 wt %) and is LREE depleted relative to the mesosome dykes.

Melanosome textures and mineral assemblages, in combination with constraints from dehydration melting experiments (Beard & Lofgren, 1991), indicate the following reactions with progressive melting at low pressures:

$$\text{Hbl} + \text{Pl} \pm \text{Qtz} = \text{Cpx} \pm \text{Opx} + \text{Ilm} + \text{Mag} + \text{Melt} \quad (1)$$

$$\text{Pl} + \text{Cpx} + \text{Opx} + \text{Ilm} + \text{Mag} = \text{Melt}. \quad (2)$$

Reaction (1) describes the breakdown of an amphibolite

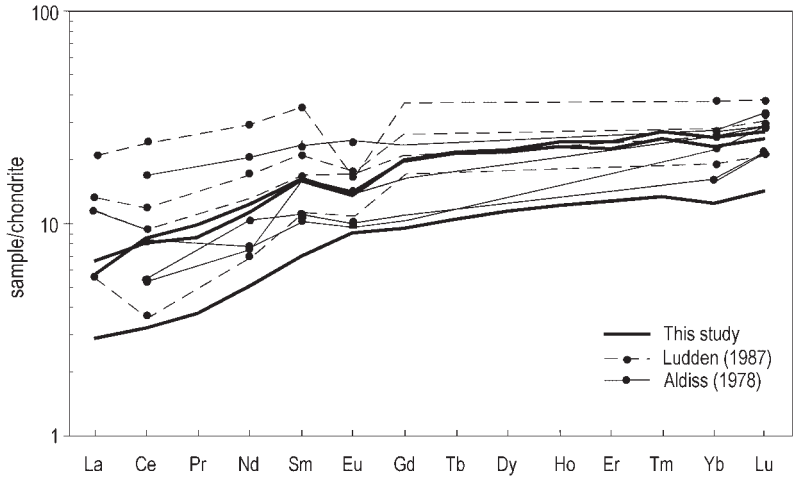

Fig. 5. Chondrite-normalized REE element plots of plagiogranite lithologies from this study and other areas in the Troodos ophiolite (Aldiss, 1978; J. Ludden, unpublished data, 1987). ●, elements that have been analysed (Aldiss and Ludden data only).

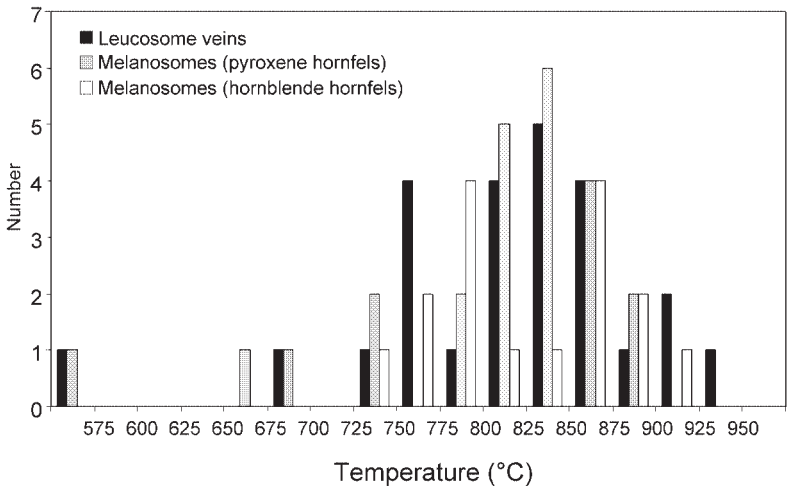

Fig. 6. Histogram of amphibole equilibration temperatures calculated using the amphibole–plagioclase thermometer of Holland & Blundy (1994). Data from this study and Gillis & Roberts (1999).

assemblage to form a tonalitic melt and a granulite restite. Reaction (2) records the partial melting of the pyroxene hornfels whereby plagioclase is the principal reactant.

Conditions of partial melting constrained from experimental studies

A wide range of experimental studies have investigated the partial melting of mafic amphibolites, primarily with the aim of understanding melting processes in the lower continental crust and the generation of tonalitic melts (e.g. Spulber & Rutherford, 1983; Rushmer, 1991; Wolf & Wyllie, 1994). Of these, the low-pressure (1 kbar) experiments of Beard & Lofgren (1991) are most relevant to this study as their starting material was composed of hydrous metamorphic mineralogies and bulk compositions similar to that of the basal sheeted dykes. These experiments were conducted at both water-saturated (unlimited external water supply) and water-undersaturated (no external water added) conditions. For the latter case, which is hereafter called dehydration melting, hydrous minerals break down to form a hydrous melt and an anhydrous mineral assemblage (Beard & Lofgren, 1991). The oxygen fugacity (f_{O_2}) was between the haematite–magnetite and nickel–nickel oxide buffers. The melting assemblages for the dehydration melting experiments included orthopyroxene, clinopyroxene,

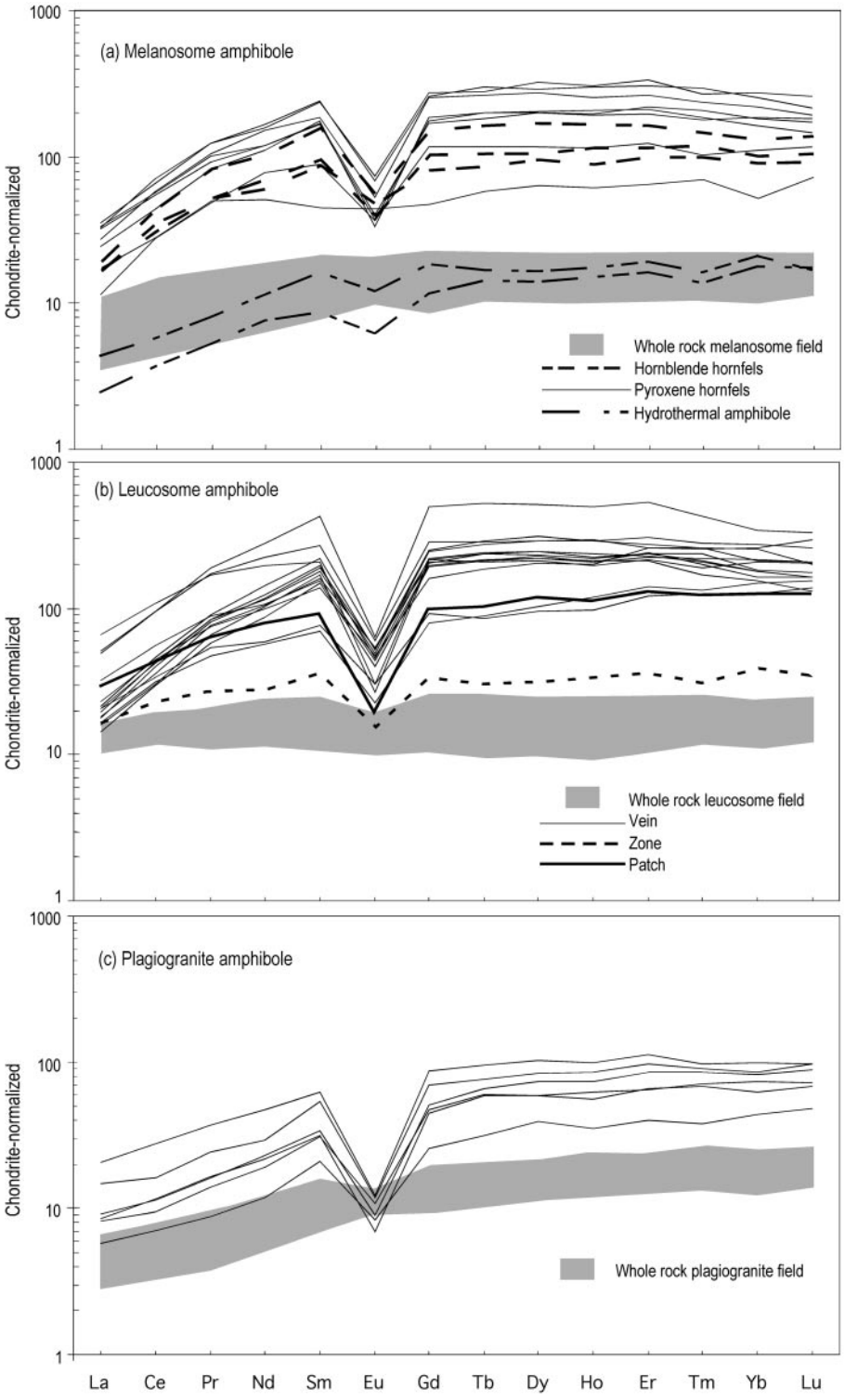

Fig. 7. Chondrite-normalized REE element plots of amphibole hosted in: (a) melanosomes; (b) leucosomes; (c) plagiogranites [chondritic values from Anders & Grevesse (1989)].

plagioclase, quartz, and magnetite and ilmenite; the water-saturated experiments also contained amphibole at low melt fractions. Both sets of experiments produced melts in which the SiO_2 contents decreased and Al_2O_3,

Fe_2O_3, CaO and MgO contents increased as temperature rose (850–1000°C) and melting progressed (up to 38% melting) (Fig. 3) (Beard & Lofgren, 1991).

Based on these experiments, we conclude that partial melting within the contact aureole proceeded at water-undersaturated conditions for the following reasons. First, leucosome compositions from this study most closely match the melts produced by dehydration melting (Fig. 3). By analogy with these experiments, the leucosomes represent melts extracted from the melanosome at different stages of melting such that the most siliceous melts were amongst the first to form. It must be kept in mind, however, that these chemical trends also probably reflect the amalgamation and partial crystallization of magmas, as well as crystal accumulation, as they migrate through the fracture network. Second, mineral modes of the experimental residual solids are similar to that for the melanosome pyroxene hornfels, except that they are more enriched in amphibole and quartz, which is consistent with these phases having formed by crystallization from trapped melt (see above). It should be noted that the coexistence of quartz and magnetite in the absence of olivine is indicative that the system in Troodos was above the quartz–fayalite–magnetite (QFM) buffer, which is generally similar to experimental conditions.

REE modelling of the melting process

Melanosomes and leucosomes show some differences in REE contents and patterns relative to mesosomes (Fig. 4d–f). Equilibrium melting models do not result in a good match between the compositions of melt and residue and those of leucosomes and melanosomes, respectively (Fig. 8a–d). Fractional melting would lead to greater differences in composition between melts and residues and thus fit the data even more poorly.

Textural criteria and amphibole trace element geochemistry suggest that, at least in some instances, melt was trapped in the hornfels and that melt–matrix separation was inefficient. Retention of some melt in the residue during melting would lead to the bulk distribution coefficient of the residue becoming closer to unity ($D_{melt} = 1$) and thus diminish leucosome–melanosome fractionation. As a consequence, the resulting residue would be significantly less depleted than one from which all melt was extracted.

Consideration of the geological context of partial melting suggests that models that assume perfect crystal–melt equilibrium are inappropriate. This is because the duration of melting within the contact aureole was probably too short to achieve full equilibrium between melt and solid before melt extraction. Melt and matrix can only reach equilibrium if either volume diffusion within minerals is fast compared with the time scale of melt extraction or complete recrystallization occurs. Assuming a full spreading rate of 5–10 cm/year and an AMC width of 1 km, a rock makes up part of the roof zone for a maximum of 10–20 kyr. However, the duration of melting events in the roof is probably much shorter than this, on the time scale of eruptive cycles (i.e. years to centuries; see discussion below). The diffusion rates of the REE at 900°C in clinopyroxene (the major source of REE) are $\sim 10^{-20}$ cm^2/s (extrapolating from higher temperatures; Sneeringer *et al.*, 1984), giving a characteristic diffusion distance of <1 μm in 20 kyr. Grain sizes in the melanosomes range from 20 to 150 μm; thus, equilibrium could not be achieved via diffusion. Recrystallization clearly occurred to produce the granular, hornfelsic, textures. However, the bimodal grain size of plagioclase suggests that recrystallization was not pervasive, indicating that complete equilibrium was not achieved.

To demonstrate the effects of disequilibrium during partial melting, models for this process are shown in Fig. 8e–h. Disequilibrium melting models assume that the concentration of an element in a melt is simply controlled by its concentration in the constituent minerals and the relative proportions in which they dissolve into the melt (Allègre & Minster, 1978; Prinzhofer & Allègre, 1985). The disequilibrium melting models presented here predict REE concentrations that are comparable with those of the leucosome and melanosomes using both andesite and rhyolite distribution coefficients (Fig. 8e–h). It is necessary to view these similarities with some caution because: (1) leucosomes probably do not represent initial melt compositions but have probably undergone some degree of partial crystallization and/or crystal accumulation; (2) some melanosomes contain trapped melt; (3) some recrystallization, and thus re-equilibration, probably did occur. Despite this, disequilibrium melting is a viable end-member mechanism.

Mass balance constraints on the extent of melting

The mass fraction of partial melting (F) of the contact aureole has been estimated using the mass balance equation $C_O = FC_L + (1 - F)C_R$, in which the average dyke is the source value (C_O), the average leucosome vein is the melt composition (C_L), and specific melanosome samples are residuum values (C_R) (Prinzhofer & Allègre, 1985). Results for the major elements that are strongly partitioned between the melanosomes and mesosomes (CaO, MgO, Al_2O_3) (Fig. 3) indicate that some hornfelses lost no melt whereas others underwent up to 50% melt extraction. Lack of geochemical evidence for melt extraction does not, however, require that no melting occurred. If it is assumed that melanosome samples with SiO_2 contents less than the average dyke value do not contain trapped melt, F ranges from 12 to 41%, with a

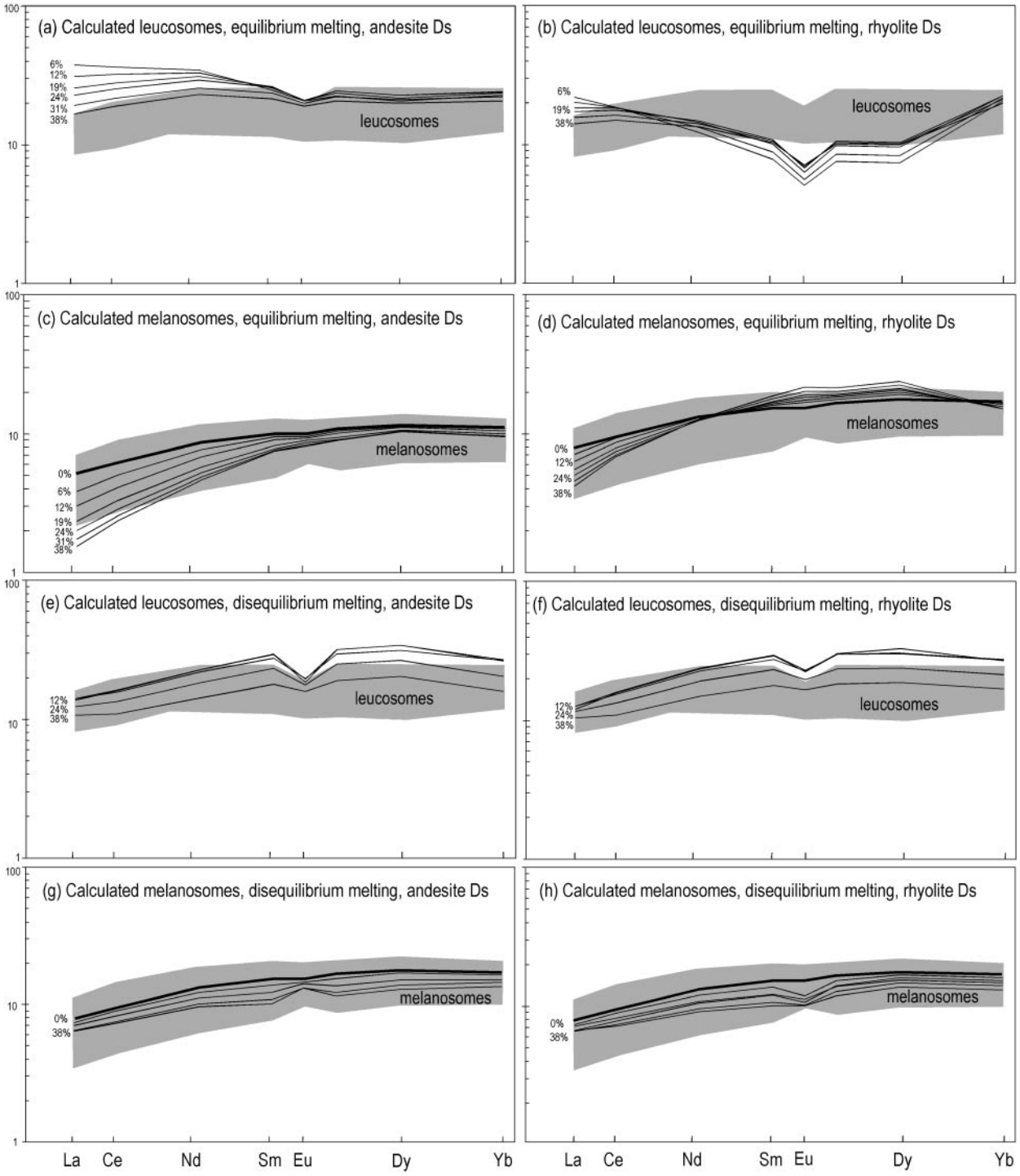

Fig. 8. Results of equilibrium (a)–(d) and disequilibrium (e)–(h) melting models. Mineral–melt distribution coefficients (*D* values) for both andesitic and rhyolitic compositions (Table 3) were used to bracket the broad range in leucosome compositions. Bulk *D* values between the melt and residual solids were calculated using the mineral modes and melt fractions produced by the dehydration melting experiments for sample 478 [shown in fig. 2 of Beard & Lofgren (1991)]. In all models, an average dyke was used as the starting composition [indicated by a bold line labelled 0% in (c), (d), (g) and (h)] and non-modal melting was assumed. Grey shaded fields show the compositional range of either whole-rock leucosome or melanosome samples. A limitation of these models is that very few of the *D* values reported in Table 3 were experimentally derived and the published database for *D* values for chemically evolved melts is rather limited.

*Table 3: Distribution coefficients used in melting models**

Mineral	Melt composition	La	Ce	Nd	Sm	Eu	Dy	Yb	Reference
Plagioclase	Andesite	0·111	0·086	0·057	0·035	0·635	0·018	0·018	Dunn & Sen (1994)
Clinopyroxene	Andesite	0·28	0·47	0·86	1·6	1·1	*2·3*	1	Bacon & Druitt (1988)
Orthopyroxene	Andesite	0·002	0·005	0·076	0·02	0·056	0·275	0·655	Dunn & Sen (1994)
Plagioclase	Rhyolite	0·3	0·22	0·19	0·12	2	*0·11*	0·1	Bacon & Druitt (1988)
Clinopyroxene	Rhyolite	0·49	1·1	2·7	5·5	*6·4*	7·1	2·1	Sisson (1991)
Orthopyroxene	Rhyolite	0·002	0·006	0·03	0·09	*0·15*	0·52	0·48	Sisson (1991)
Ilmenite	All	0·007	*0·007*	*0·008*	0·009	0·009	*0·017*	*0·026*	Nielsen *et al.* (1992)
Magnetite	All	0·003	0	*0·01*	0·007	0·006	*0·01*	*0·02*	Nielsen *et al.* (1992)

*Values in italics were extrapolated from the adjacent elements.

mean of 29% ($n = 8$). Similar degrees of melting are obtained using the LREE but higher (mean 55%) F values are indicated by the HREE. Although both pyroxene and hornblende hornfelses show evidence of melting, it is more common in the pyroxene hornfelses, which generally crop out closest to the gabbros.

DISCUSSION

Partial melting in the roof of an oceanic magma chamber

The contact aureole is interpreted as a conductive boundary layer that evolved within the dynamic roof zone of a MOR magma chamber (Gillis & Roberts, 1999). Geological constraints show that the magma–hydrothermal transition migrated vertically in response to changing thermal conditions imposed by the magmatic system, on a time scale of an eruptive cycle that spans years to centuries (Gillis, 2002). Downward migration led to progressive hydration and alteration of the basal sheeted dykes and uppermost gabbros at greenschist to lower amphibolite conditions. During periods of enhanced magmatic heat flux, the basal dykes underwent prograde devolatilization reactions at amphibolite- to granulite-facies conditions, releasing fluids that acted to lower the solidus in the vicinity of the contact aureole. As this heat flux diminished, the magma–hydrothermal boundary deepened again into the gabbros and transient cracking of the conductive boundary layer allowed the ingress of seawater-derived hydrothermal fluids and the escape of magmatic volatiles.

The distribution of leucosomes within the contact aureole, in conjunction with the compositions and textures of the hornfelses, indicates that partial melting was generally restricted to the ~10 m closest to the gabbros and that melting and melt extraction was heterogeneous. Given the uncertainties of the partial melting calculations, the volume of leucosome present in these outcrops (~15%) is in reasonable agreement with the predicted average degree of melting from mass balance considerations (~30%). In contact aureoles, the most effective driving force for melt segregation comes from the melting reaction itself. Dehydration partial melting will create high pore pressures as a result of the positive volume change of melting and is a potential cause of brittle failure. Embrittlement would also be promoted by the thermal stresses of magmatic intrusion (Lister, 1974) and dilatant stresses caused by devolatilization reactions (Dutrow & Norton, 1995; Hanson, 1995). Melt overpressures would promote melt transport via porous flow through the mineral–melt aggregate into lower-pressure tensile fractures (Sleep, 1988; Petford, 1995). It is likely that melt segregation is episodic such that fracturing and melt drainage reduces overpressures near fractures. This may in turn reduce melt migration until pressure is later enhanced by further melting (Clemens & Mawer, 1992; Rushmer, 1996). At a fast-spreading ridge, the cyclicity of melt formation and extraction could be triggered by magmatic events such as replenishment of the AMC and dyke injection (Sleep, 1988; Petford, 1995).

The contact aureole evolved within a dynamic setting where the magma–hydrothermal transition migrated vertically. This means that temperatures within the conductive boundary layer were not steady state and fluctuated above and below the solidus (~875°C, Beard & Lofgren, 1991). The amount of time required to initiate melting within the contact aureole has been assessed using equation (1) of Irvine (1970) (modified from Carslaw & Jaeger, 1959). These calculations assume that magma at the base of the contact aureole was a constant heat source at 1000°C, the thermal diffusivity of the roof rock was $0{\cdot}714 \times 10^{-6}$ m^2/s, and initial roof rock temperature was 500°C. Results show that melting temperatures would be achieved very rapidly. For example, it would take 5 years to reach the solidus 5 m from the lower

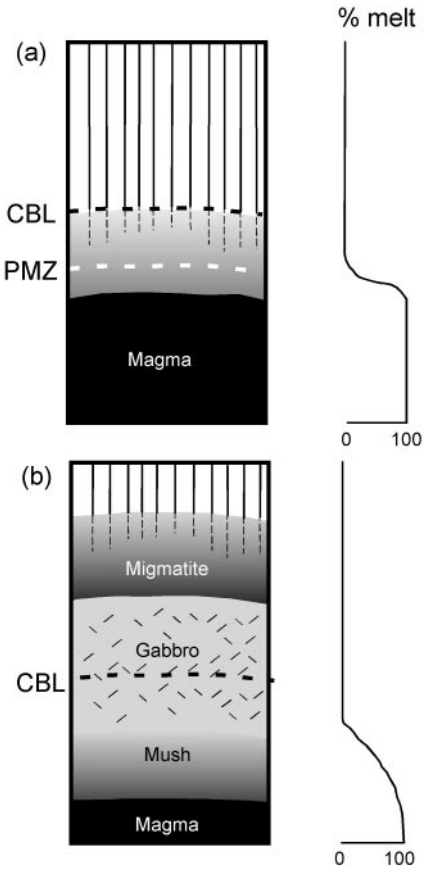

Fig. 9. Schematic diagram showing two end-member states of an axial magma chamber roof. (a) The AMC resides at the base of the sheeted dyke complex as a result of recent magma replenishment. A 10–30 m conductive boundary layer (CBL) overlies the AMC; within this region, hydrothermally altered sheeted dykes are thermally metamorphosed and partially melted. (b) The AMC resides in the gabbro sequence. The CBL overlies a crystal mush zone, which in turn is overlain by a narrow zone of migmatites that developed when the AMC was replenished, as shown in (a). The black dashed line marks the top of the CBL; the white dashed line marks the top of the partially melted zone (PMZ).

contact, 10 years 12 m from the contact, and 70 years 30 m from the contact. Less time would be required if wall rock temperatures were higher and/or if the magmatic heat source was hotter. Alternatively, longer times would be required if hydrothermal heat extraction was efficient. Hence, melting temperatures could be achieved on similar time scales to eruptive cycles.

We suggest a history for the conductive boundary layer as follows. A magmatic event, such as AMC replenishment, caused the magma–hydrothermal boundary to migrate upwards into the base of the sheeted dyke complex (Fig. 9a). This rapid input of thermal energy elevated the roof-rock temperature and promoted the recrystallization of hydrothermally altered dykes to high-grade hornfels within a narrow contact aureole (<30 m). When supersolidus temperatures were maintained at the base of the conductive boundary layer for years to tens of years, partial melting of the hornfels generated leucocratic melt. The limited duration of the thermal excursion resulted in disequilibrium partial melting and highly imperfect melt segregation within the contact aureole. Where melting was greatest (>40%?) and the underlying region was partially molten, the melt–solid mixture probably became disaggregated and incorporated into the gabbros (i.e. assimilation occurred). The presence of numerous hornfelsic xenoliths in the uppermost gabbros provides clear evidence that dykes were stoped, recrystallized and partially assimilated into the magmatic system at very high temperatures. Leucocratic vein networks that cross-cut the uppermost gabbros could be the product of partial melting of these assimilated dykes. Solidification of the AMC drove the conductive boundary layer into the gabbros (Fig. 9b) until the next magmatic heat flux perturbed the system (Fig. 9a).

Implications of roof melting in fast-spreading ridge magma chambers

Geophysical surveys show that axial magma chambers at fast-spreading ridges form thin magma sills (<100 m thick) that are 250–1500 m wide and reside 1–2 km beneath the sea floor (e.g. Detrick *et al.*, 1987; Kent *et al.*, 1993). These properties appear to be unrelated to morphological features indicative of magma supply from the mantle (e.g. axial volume and depth) and are more closely related to shorter-term eruptive cycles ($10–10^2$ years) (Hussenoeder *et al.*, 1996; Hooft *et al.*, 1997; Macdonald, 1998). The internal properties of magma sills are less well constrained. Recent studies suggest that many AMCs are best described as 'mushes' (mixtures of melt and crystals) with crystal contents as high as, or higher than, 80% in many places (Hussenoeder *et al.*, 1996; Collier & Singh, 1997; Singh *et al.*, 1998). Our knowledge of along-axis variations in the melt to mush proportions is limited to the southern EPR, near 14°00′S (Singh *et al.*, 1998). Here, the AMC is generally thin (~50 m) and crystal rich (40–60% crystals) but three discrete 2–4 km long pure melt sections also occur at a spacing of 15–20 km (Singh *et al.*, 1998). Although the data are not robust, there are indications from other areas along the EPR that thicker sills have lower crystal contents (Hussenoeder *et al.*, 1996) and crystal mushes can be concentrated beneath thin zones of molten (<30% crystals) material (Collier & Singh, 1997) or overlie zones of high crystallinity (>60% crystals) (Collier & Singh, 1998). An inference that has been drawn from these studies is that the common state of AMCs at fast-spreading ridges is one of uneruptable crystal mushes, which at a specific time and place, are transformed into a melt-rich state by replenishment of magma (Singh *et al.*, 1998).

This study documents the existence of anatectic migmatites within the conductive boundary layer of a MOR magma chamber and points to an alternative view of crystal-rich AMCs. Some part of the low melt fraction AMCs could equally well be composed of partially melted upper crust that resides within a conductive boundary layer rather than newly accreted melt and crystals. This is because the AMC roof could be partially molten as a result of its hydrous nature whereas the underlying gabbros reside at near-solidus conditions (e.g. Collier & Singh, 1998). Partial assimilation of AMC roofs would lead to the recycling of upper-crustal material into the gabbroic sequence and affect the chemistry of MOR basalts erupted at fast-spreading ridges (e.g. Michael & Schilling, 1989; Chaussidon & Marty, 1995; Michael & Cornell, 1998).

ACKNOWLEDGEMENTS

This manuscript benefited from informal reviews by, and discussions with, M. O'Hara and Y. Nui, and formal reviews by F. Boudier and B. Murton. Laboratory assistance by J. Fan and C. Lewis (ICP-MS laboratories), L. Shi (microprobe) and P. McDade (scanning electron microscopy) are gratefully acknowledged. J. Ludden is thanked for providing unpublished data. This paper was prepared while K.M.G. was a guest at Cardiff University. This research was supported by an NSERC Research Grant to K.M.G.; L.A.C. acknowledges support from Cardiff University.

REFERENCES

Aldiss, C. R. (1978). Granitic rocks of ophiolites. Ph.D. thesis, Open University, Milton Keynes, 198 pp.

Allègre, C. J. & Minster, J. F. (1978). Quantitative models of trace element behaviour in magmatic processes. *Earth and Planetary Science Letters* **38**, 1–25.

Anders, E. & Grevesse, N. (1989). Abundances of the elements: meteoritic and solar. *Geochimica et Cosmochimica Acta* **53**, 197–214.

Bacon, C. R. & Druitt, T. H. (1988). Compositional evolution of the zoned calcalkaline magma chamber of Mount Mazama, Crater Lake, Oregon. *Contributions to Mineralogy and Petrology* **98**, 224–256.

Beard, J. S. (1990). Partial melting of metabasites in the contact aureoles of gabbroic plutons in the Smartville Complex, Sierra Nevada, California. In: Anderson, J. L. (ed.) *The Nature and Origin of Cordilleran Magmatism. Geological Society of America Memoir* **174**, 303–313.

Beard, J. S. & Lofgren, G. E. (1991). Dehydration melting and water-saturated melting of basaltic and andesitic greenstones and amphibolites. *Journal of Petrology* **32**, 365–401.

Blome, C. D. & Irwin, W. P. (1985). Equivalent radiolarian ages from ophiolitic terranes of Cyprus and Oman. *Geology* **13**, 401–404.

Boudier, F., Nicolas, A. & Ildefonse, B. (1996). Magma chambers in the Oman Ophiolite: fed from the top and the bottom. *Earth and Planetary Science Letters* **144**, 239–250.

Boudier, F., Godard, M. & Armbruster, C. (2000). Significance of gabbronorite occurrence in the crustal section of the Semail ophiolite. *Marine Geophysical Researches* **21**, 307–326.

Busch, W., Schneider, G. & Mehnert, K. R. (1974). Initial melting at grain boundaries. Part II: melting in rocks of granitic, quartz dioritic, and tonalitic composition. *Neues Jahrbuch für Mineralogie, Monatshefte* 345–370.

Cann, J. R., Strens, M. R. & Rice, A. (1985). A simple magma-driven thermal balance model for the formation of volcanogenic massive sulphides. *Earth and Planetary Science Letters* **76**, 123–134.

Carslaw, H. S. & Jaeger, J. C. (1959). *Conduction of Heat in Solids*. London: Oxford University Press, p. 510.

Chaussidon, M. & Marty, B. (1995). Primitive boron isotope composition of the mantle. *Science* **269**, 383–386.

Chen, Z. (1999). Inter-element fractionation and correction in laser ablation inductively coupled plasma mass spectrometry. *Journal of Analytical and Atomic Spectrometry* **14**, 1823–1828.

Clemens, J. D. & Mawer, C. K. (1992). Granitic magma transport by fracture propagation. *Tectonophysics* **204**, 339–360.

Collier, J. S. & Singh, S. C. (1997). Detailed structure of the top of the melt body beneath the East Pacific Rise at 9°40′N from waveform inversion of seismic reflection data. *Journal of Geophysical Research* **102**, 20287–20304.

Collier, J. S. & Singh, S. C. (1998). A seismic inversion study of the axial magma chamber reflector beneath the East Pacific Rise near 10°N. In: Mills, R. A. & Harrison, K. (eds) *Modern Ocean Floor Processes and the Geological Record. Geological Society, London, Special Publications* **148**, 17–28.

Delaney, J. R., Kelley, D. S., Lilley, M. D., Butterfield, D. A., Baross, J. A., Wilcock, W. S. D., Embley, R. W. & Summit, M. (1998). The quantum event of oceanic crustal accretion: impacts of diking at mid-ocean ridges. *Science* **281**, 222–230.

Detrick, R. S., Buhl, P., Vera, E., Mutter, J., Orcutt, J., Madsen, J. & Brocher, T. (1987). Multichannel seismic imaging of a crustal magma chamber along the East Pacific Rise. *Nature* **326**, 35–41.

Dunn, T. & Sen, C. (1994). Mineral/matrix partition coefficients for orthopyroxene, plagioclase, and olivine in basaltic to andesitic systems: a combined analytical and experimental study. *Geochimica et Cosmochimica Acta* **58**, 717–733.

Dutrow, B. & Norton, D. (1995). Evolution of fluid pressure and fracture propagation during contact metamorphism. *Journal of Metamorphic Geology* **13**, 677–686.

Gillis, K. M. (2002). The rootzone of an ancient hydrothermal system exposed in the Troodos ophiolite, Cyprus. *Journal of Geology* **110**, 57–74.

Gillis, K. M. & Roberts, M. (1999). Cracking at the magma–hydrothermal transition: evidence from the Troodos ophiolite. *Earth and Planetary Science Letters* **169**, 227–244.

Hanson, R. B. (1995). The hydrodynamics of contact metamorphism. *Geological Society of America Bulletin* **107**, 595–611.

Holland, T. & Blundy, J. (1994). Non-ideal interactions in calcic amphiboles and their bearing on amphibole–plagioclase thermometry. *Contributions to Mineralogy and Petrology* **116**, 433–447.

Hooft, E. E. E., Detrick, R. S. & Kent, G. M. (1997). Seismic structure and indicators of magma budget along the Southern East Pacific Rise. *Journal of Geophysical Research* **102**, 27319–37340.

Hussenoeder, S. A., Collins, J. A., Kent, G. M., Detrick, R. S. & Group, T. (1996). Seismic analysis of the axial magma chamber reflector along the southern East Pacific Rise from conventional reflection profiling. *Journal of Geophysical Research* **101**, 22087–22105.

Irvine, T. N. (1970). Heat transfer during solidification of layered intrusions: sheets and sills. *Canadian Journal of Earth Science* **7**, 1031–1061.

Jurewicz, S. R. & Watson, E. B. (1984). Distribution of partial melt in a felsic system: the importance of surface energy. *Contributions to Mineralogy and Petrology* **85**, 25–29.

Kane, J. S. (1998). A history of the development and certification of NIST glass SRMs 610–617. *Geostandards Newsletter* **22**, 7–13.

Kent, G. M., Harding, A. J. & Orcutt, J. A. (1993). Distribution of magma beneath the East Pacific Rise between the Clipperton Transform and the 9°17′N deval from forward modeling of common depth point data. *Journal of Geophysical Research* **98**, 13945–13969.

Lister, C. R. B. (1974). On the penetration of water into hot rock. *Geophysical Journal of the Royal Astronomical Society* **39**, 465–509.

Lowell, R. P. & Burnell, D. K. (1991). Mathematical modeling of conductive heat transfer from a freezing, convecting magma chamber to a single-pass hydrothermal system: implications for seafloor black smokers. *Earth and Planetary Science Letters* **104**, 59–69.

Macdonald, K. C. (1998). Linkages between faulting, volcanism, hydrothermal activity and segmentation on fast spreading centers. In: Buck, W. R., Delaney, P. T., Karson, J. A. & Lagabrielle, Y. (eds) *Faulting and Magmatism at Mid-Ocean Ridges. Geophysical Monograph, American Geophysical Union* **106**, 27–58.

Malpas, J. (1990). Crustal accretionary processes in the Troodos ophiolite, Cyprus: evidence from field mapping and deep crustal drilling. In: Malpas, J., Moores, E. M., Panayiotou, A. & Xenophontos, C. (eds) *Ophiolites: Ocean Crustal Analogues*. Nicosia: Cyprus Geological Survey Department, pp. 65–74.

Malpas, J. & Brace, T. (1987). *The Geology of Pano Amiandos–Palekhori Area, Cyprus*. Nicosia: Cyprus Geological Survey Department.

Michael, P. J. & Cornell, W. C. (1998). Influence of spreading rate and magma supply on crystallisation and assimilation beneath mid-ocean ridges: evidence from chlorine and major element chemistry of mid-ocean ridge basalts. *Journal of Geophysical Research* **103**, 18325–18356.

Michael, P. J. & Schilling, J.-G. (1989). Chlorine in mid-ocean ridge magmas: evidence for assimilation of seawater-influenced components. *Geochimica et Cosmochimica Acta* **53**, 3131–3143.

Miyashiro, A. (1973). The Troodos ophiolitic complex was probably formed in an island arc. *Earth and Planetary Science Letters* **19**, 218–224.

Mukasa, S. B. & Ludden, J. N. (1987). Uranium–lead isotopic ages of plagiogranites from the Troodos ophiolite, Cyprus and their tectonic significance. *Geology* **15**, 825–828.

Nasland, H. R. (1986). Disequilibrium partial melting and rheomorphic layer formation in the contact aureole of the Basistoppen sill, East Greenland. *Contributions to Mineralogy and Petrology* **93**, 359–367.

Nicolas, A. (1992). Kinematics in magmatic rocks with special reference to gabbros. *Journal of Petrology* **33**, 891–915.

Nicolas, A. & Boudier, F. (1991). Rooting of the sheeted dike complex in the Oman Ophiolite. In: Peters, T., Nicolas, A. & Coleman, R. G. (eds) *Ophiolite Genesis and Evolution of the Oceanic Lithosphere*. Dordrecht: Kluwer Academic; Sultanate of Oman: Ministry of Petroleum and Minerals, pp. 39–54.

Nielsen, R. L., Gallahan, W. E. & Newberger, F. (1992). Experimentally determined mineral–melt partition coefficients for Sc, Y and REE for olivine, orthopyroxene, pigeonite, magnetite and ilmenite. *Contributions to Mineralogy and Petrology* **110**, 488–499.

Pallister, J. S. & Hopson, C. A. (1981). Samail ophiolite plutonic suite: field relations, phase variation, cryptic variation and layering, and a model of a spreading ridge magma chamber. *Journal of Geophysical Research* **86**, 2593–2644.

Pattison, D. R. M. & Harte, B. (1988). Evolution of structurally contrasting anatectic migmatites in the 3-kbar Ballachulish aureole, Scotland. *Journal of Metamorphic Petrology* **6**, 475–494.

Pearce, J. A., Lippard, S. J. & Roberts, S. (1984). Characteristics and tectonic significance of supra-subduction zone ophiolites. In: Kokelaar, B. P. & Howeels, M. F. (eds) *Marginal Basin Geology: Volcanic and Associated Sedimentary and Tectonic Processes in Modern and Ancient Marginal Basins. Geological Society, London, Special Publication* **16**, 77–94.

Pedersen, R. B. (1986). The nature and significance of magma chamber margins in ophiolites: examples from the Norwegian Caledonides. *Earth and Planetary Science Letters* **77**, 100–112.

Pedersen, R. B. & Malpas, J. (1984). The origin of oceanic plagiogranites from the Karmoy ophiolite, Western Norway. *Contributions to Mineralogy and Petrology* **88**, 36–52.

Petford, N. (1995). Segregation of tonalitic–trondhjemitic melts in the continental crust: the mantle connection. *Journal of Geophysical Research* **100**, 15735–15743.

Phipps Morgan, J. & Chen, Y. J. (1993). The genesis of oceanic crust: magma injection, hydrothermal circulation, and crustal flow. *Journal of Geophysical Research* **98**, 6283–6297.

Prinzhofer, A. & Allègre, C. J. (1985). Residual peridotites and the mechanisms of partial melting. *Earth and Planetary Science Letters* **74**, 251–265.

Quick, J. E. & Denlinger, R. P. (1993). Ductile deformation and the origin of layered gabbro in ophiolites. *Journal of Geophysical Research* **98**, 14015–14027.

Rothery, D. A. (1983). The base of a sheeted dyke complex, Oman ophiolite: implications for magma chambers at oceanic spreading axes. *Journal of the Geological Society, London* **140**, 287–296.

Rushmer, T. (1991). Partial melting of two amphibolites: contrasting experimental results under fluid-absent conditions. *Contributions to Mineralogy and Petrology* **107**, 41–59.

Rushmer, T. (1996). Melt segregation in the lower crust: how have experiments helped us? *Transactions of the Royal Society of Edinburgh: Earth Sciences* **87**, 73–83.

Sawyer, E. W. (1999). Criteria for the recognition of partial melting. *Physics and Chemistry of the Earth* **24**, 269–279.

Singh, S. C., Kent, G. M., Collier, J. S., Harding, A. J. & Orcutt, J. A. (1998). Melt to mush variations in crustal magma chamber properties along the ridge crest at the southern East Pacific Rise. *Nature* **394**, 874–878.

Sisson, T. W. (1991). Pyroxene–high silica rhyolite trace element partition coefficients measured by ion microprobe. *Geochimica et Cosmochimica Acta* **55**, 1575–1585.

Sleep, N. H. (1988). Tapping of melt by veins and dikes. *Journal of Geophysical Research* **93**, 10255–10272.

Sneeringer, M., Hart, S. R. & Shimizu, N. (1984). Strontium and samarium diffusion in diopside. *Geochimica et Cosmochimica Acta* **48**, 1589–1608.

Spulber, S. D. & Rutherford, M. J. (1983). The origin of rhyolite and plagiogranite in oceanic crust: an experimental study. *Journal of Petrology* **24**, 1–25.

van Everdingen, D. A. & Cawood, P. A. (1995). Dyke domains in the Mitsero graben, Troodos ophiolite, Cyprus: an off-axis model for graben formation at a spreading centre. *Journal of the Geological Society, London* **152**, 923–932.

Varga, R. J. & Moores, E. M. (1990). Intermittent magmatic spreading and tectonic extension in the Troodos Ophiolite: implications for exploration of black smoker-type ore deposits. In: Malpas, J., Moores, E. M., Panayiotou, A. & Xenophontos, C. (eds) *Ophiolites: Oceanic Crustal Analogues*. Nicosia: Cyprus Geological Survey Department, pp. 53–64.

Varga, R. J., Gee, J. S., Bettison-Varga, L., Anderson, R. S. & Johnson, C. L. (1999). Early establishment of seafloor hydrothermal systems

during structural extension: paleomagnetic evidence from the Troodos Ophiolite. *Earth and Planetary Science Letters* **171**, 221–235.

Vernon, R. H. & Collins, W. J. (1988). Igneous microstructures in migmatites. *Geology* **16**, 1126–1129.

Wilcock, W. S. D. & Delaney, J. R. (1996). Mid-ocean ridge sulfide deposits: evidence for heat extraction from magma chambers or cracking fronts? *Earth and Planetary Science Letters* **145**, 49–64.

Wolf, M. B. & Wyllie, P. J. (1991). Dehydration-melting of solid amphibolite at 10 kbar: textural development, liquid interconnectivity and applications to the segregation of magmas. *Mineralogy and Petrology* **44**, 151–179.

Wolf, M. B. & Wyllie, P. J. (1994). Dehydration melting of amphibolite at 10 kbar: the effects of temperature and time. *Contributions to Mineralogy and Petrology* **115**, 369–383.